AIAA-2002-0240

EFFECT OF INTERCYCLE ICE ACCRETIONS ON AIRFOIL PERFORMANCE

Andy P. Broeren,* Harold E. Addy, Jr.† and Michael B. Bragg‡

University of Illinois at Urbana-Champaign, Urbana, Illinois 61801
NASA Glenn Research Center at Lewis Field, Cleveland, Ohio 44135

ABSTRACT

This paper presents the results of an experimental study designed to characterize and evaluate the aerodynamic performance penalties of residual and intercycle ice accretions that result from the cyclic operation of a typical aircraft deicing system. Icing wind tunnel tests were carried out on a 36-inch chord NACA 23012 airfoil section equipped with a pneumatic deicer for several different cloud conditions modeled after FAR 25 Appendix C. Results from the icing tests showed that the intercycle ice accretions were much more severe in terms of size and shape than the residual ice accretions. Molds of selected intercycle ice shapes were made and converted to castings that were attached to the leading edge of a 36-inch chord NACA 23012 airfoil model for aerodynamic testing. The aerodynamic testing revealed that the intercycle ice shapes caused a significant performance degradation. Maximum lift coefficients were typically reduced about 60% from 1.8 (clean) to 0.7 (iced) and stall angles were reduced from 17 deg. (clean) to 9 deg. (iced). Changes in the Reynolds number (from 2.0×10^6 to 10.5×10^6) and Mach number (from 0.10 to 0.28) did not significantly affect the iced-airfoil performance coefficients.

NOMENCLATURE

α	Airfoil angle of attack
α_{stall}	Stalling angle of attack, coincident with $C_{l,max}$
c	Airfoil chord length
C_d	Drag coefficient
C_l	Lift coefficient
$C_{l,\alpha}$	Lift-curve slope
$C_{l,max}$	Maximum lift coefficient, coincident with α_{stall}
C_m	Quarter-chord pitching-moment coefficient
k	Ice roughness height or thickness
Ma	Freestream Mach number
Re	Reynolds number based on chord
x	Chordwise position along airfoil
y	Normal position from airfoil chord line
CM	Continuous Maximum icing condition
IM	Intermittent Maximum icing condition
LWC	Liquid water content
MVD	Median volumetric diameter

INTRODUCTION

The cyclic operation of typical pneumatic aircraft deicing systems leads to the formation of residual and intercycle ice accretions. For example, pneumatic boots are usually inflated and deflated at either one-minute or three-minute intervals, depending upon the severity of icing. The ice accretion present on the deicer surface just prior to its initial activation is the "preactivation" ice. After the system has been cycled a sufficient number of times, the periodic activation and ice accretion cycle reaches steady state. After steady state has been reached, "inter-cycle" ice refers to the ice shape as it exists immediately *before* subsequent activations of the deicer. This is not to be confused with "residual" ice which refers to any ice that remains on the surface immediately *after* the deicer activation. This paper addresses the characteristics of residual and intercycle ice accretions for a given airfoil and deicing system along with the aerodynamic performance penalties of intercycle ice accretions.

The general effect of ice accretions on airfoil performance are well known—decreased lift and increased drag, and have been researched extensively for several years. Many survey papers exist, for example Lee, Kim and Bragg[1] reported on ice-shape

* Post-doctoral Research Scientist, Dept. of Aeronautical and Astronautical Eng., Univ. of Illinois, Member AIAA.
† Research Engineer, Icing Branch, NASA Glenn Research Center at Lewis Field, Member AIAA.
‡ Professor and Head, Dept. of Aeronautical and Astronautical Eng., Univ. of Illinois, Associate Fellow, AIAA.

location, size, geometry and other effects on airfoil performance. However, the case of intercycle ice is different in that data on the characteristics of the ice shapes themselves are more scarce. Shin and Bond[2] analyzed the characteristics of residual and intercycle ice accretions for several different deicing systems installed on an NACA 0012 airfoil. The reported results were for one minute cycling times and showed that the deicers generally cleaned the leading edge, leaving little residual ice. The intercycle ice, therefore, would accrete in the one minute period leading up to the deicer operation. The height of this inter-cycle ice roughness, normalized by chord, varied from approximately $k/c = 0.002$ to 0.010, depending upon the icing condition (i.e., glaze or rime) and the type of deicer. Shin and Bond[2] concluded that the intercycle ice would have an effect on airfoil and wing performance and that uniformly distributed roughness may not be an appropriate simulation of the actual intercycle ice. No aerodynamic measurements were performed during the study.

There are a small number of previous studies in the public domain that measured the aerodynamic performance effects of residual and intercycle ice accretions. Albright et al.[3] measured the drag coefficient before and after the operation of a pneumatic deicer on a NACA 65_1-215 airfoil. The general results showed that the intercycle ice (before deicer operation) caused a higher drag coefficient than the residual ice (after deicer operation), both of which were higher than for the clean airfoil. Similar research was carried out by Bowden[4] for an NACA 0011 airfoil. Bowden[4] also showed how the lift coefficient decreased as ice was accreted and then increased when the boot was cycled and the ice shed. The results of these studies were taken from a recent review of residual ice characteristics and performance penalties and the reader is encouraged to consult Reichhold and Bragg[5] for more details. While these reports provided meaningful data on the performance effects of residual and intercycle ice accretions, a major shortcoming was that the data were acquired at fixed angle of attack. Therefore, the change in the airfoil stall characteristics was not documented.

The effect of intercycle ice accretions on airfoil stalling characteristics was considered as part of a larger study by Jackson and Bragg.[6] Tracings were made of intercycle ice shapes produced on a 48-inch chord NLF-0414 airfoil for one icing cloud condition and for one-minute cycling times. These tracings were used to produce two-dimensional (i.e., no spanwise variation in cross-section) ice shape simulations that were geometrically scaled and attached to the leading edge of a 18-inch chord NLF-0414 airfoil model. While the degradation in maximum lift was on the order of 30%, the tests were conducted on a small scale model at low Reynolds number (less than 2.0×10^6). In addition, the effect of the three-dimensional nature of the intercycle ice accretions was not quantified.

The brief literature survey shows that there are valuable studies in the public domain, but more information is needed. Particularly, the effect of actual residual and intercycle ice accretions formed at one angle of attack on airfoil performance over its larger operating range is largely unknown. Recently, some questions have been raised concerning the effects of residual and inter-cycle ice for turbopropeller and piston aircraft employing pneumatic boot deicing systems.[7,8] Since little relevant data were available, the Federal Aviation Administration (FAA), in collaboration with the National Aeronautics and Space Administration (NASA) commissioned a study to assess the potential aerodynamic severity of residual and intercycle ice accretions. This effort involved researchers at the University of Illinois and BFGoodrich Aerospace Deicing and Specialty Systems Division, with participation by some aircraft manufacturers. More details on the scope of this work can be found in Riley et al.[9]

The objectives of this study were to characterize the nature of residual and intercycle ice accretions, measure the resulting aerodynamic performance penalties of selected intercycle ice accretions and determine if more detailed study was warranted. A NACA 23012 airfoil was selected for this study, since it is representative of wing airfoil sections used on some aircraft currently in operation. The airfoil was equipped with a pneumatic deicing boot provided by BFGoodrich. The intercycle ice accretions were generated in the BFGoodrich icing wind tunnel and were molded using procedures developed at the NASA Glenn Research Center. From these molds, castings were made that were attached to the leading edge of a NACA 23012 airfoil in the NASA Langley Low-Turbulence Pressure Tunnel (LTPT). Subsequent airfoil performance measurements were made over a large range of angles of attack, Reynolds and Mach numbers.

ICE ACCRETION TESTING

Experimental Arrangement

The ice accretion testing was conducted at the BFGoodrich Icing Wind Tunnel (IWT). The IWT is a closed-loop, refrigerated wind tunnel capable of air speeds of 200 mph and temperatures as low as –22 °F. The test section is 22-inches wide by 44-inches high by 60-inches long. The icing cloud in the tunnel is generated by NASA-type, atomizing nozzles mounted

in seven spray bars located in the settling chamber upstream of the test section. Cloud conditions can be set for droplet *MVD*'s from 5 to 40 microns. Liquid water contents from 0.15 to over 3.0 g/m^3 can be obtained depending upon air speed and droplet size. A cold room capable of maintaining temperatures as low as –20 °F is located adjacent to the test section.

The NACA 23012 airfoil model used for the icing tests had a 36-inch chord and 22-inch span. It was CNC machined from aluminum and was designed with a removable leading edge as shown in Fig. 1. The removable leading-edge design allowed an ice accretion to be removed intact from the test section and placed in the cold room where a mold of the ice was made. A second leading edge could then be installed on the model and further tests run. The model was mounted horizontally in the IWT and supported at each end by a one-inch thick aluminum turntable. A thermocouple was mounted on the aft portion of the model to monitor model temperature and ensure the model was at an appropriate temperature prior to initiating the test run.

Each of the two leading edges was recessed to accommodate a flush mounted BFGoodrich pneumatic deicer type 29S. The two identical deicers had five spanwise tubes, two of which were 1.25-inches wide and three that were one-inch wide, as shown in Fig. 1. The deicing system was sized and designed for the 36-inch chord, NACA 23012 airfoil flying at turboprop aircraft speeds. When installed on the model in the tunnel, the deicers were connected to a larger pneumatic deicer outside the tunnel in order to obtain the desired inflation rate. A pressure transducer provided continuous monitoring of the inflation pressure. The deicer system ran at a supply air pressure of 18 psig. A suction system was used to provide a slight vacuum to hold the deicer tubes down when not inflated. The deicer operation was computer controlled and was set up for either one-minute or three-minute cycles.

The icing conditions selected for this experiment were based on the FAR 25 Appendix C conditions and are summarized in Tables 1 and 2. They covered a range of conditions including rime, mixed, and glaze icing. Static air temperatures were –22, –4, 14, and 21 °F and the cloud droplet *MVD*'s were 20 and 40 μm. Cloud *LWC*'s from 0.15 to 0.65 g/m^3 were selected to model continuous maximum (*CM*) conditions from Appendix C, while *LWC*'s from 0.40 to 2.20 g/m^3 were used to model intermittent maximum (*IM*) conditions. Typically, an icing spray time of twelve minutes was used for the *CM* runs and a spray time of three minutes was used for the *IM* conditions.

A limited number of air speeds and model angles of attack were used. For most of the test runs, the air speed was set at the tunnel maximum of 200 mph. This corresponded to a Reynolds number of 6.5×10^6 and a Mach number of 0.27 at 14 °F. Two test runs were made at 175 mph in order to obtain the high LWC's needed for *IM* conditions. This corresponded to a Reynolds and Mach number of 5.7×10^6 and 0.24, respectively. Two angles of attack were selected for the tests, zero and four degrees.

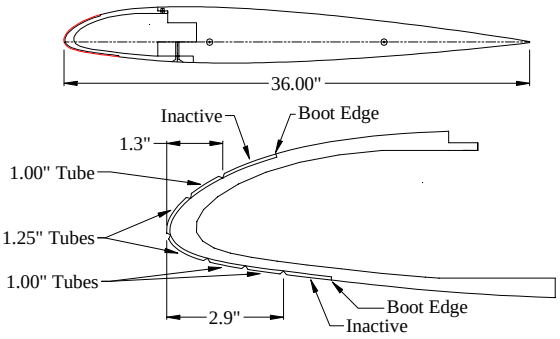

Fig. 1 NACA 23012 icing wind tunnel model with removable leading edge and deicer.

Table 1 Summary of continuous maximum icing conditions

Icing Cond.	Static Temp. (°F)	Droplet *MVD* (μm)	Cloud *LWC* (g/m^3)	Time to Activation (sec)*	Angle of Attack (deg.)	Icing Type†
A	21	20	0.65	8	0, 4	I, R
B	14	20	0.45	11	0, 4	I, R
C	–4	20	0.25	20	0, 4	I, R
D	21	40	0.25	19	0, 4	I, R
E	14	40	0.25	19	0, 4	I
F	–4	40	0.25	19	0, 4	I, R
G	–22	20	0.15	34	0	I

* Calculated using the ice detector simulation method
† I = Intercycle ice case, R = Residual ice case

Table 2 Summary of intermittent maximum icing conditions

Icing Cond.	Static Temp. (°F)	Droplet *MVD* (μm)	Cloud *LWC* (g/m^3)	Time to Activation (sec)*	Angle of Attack (deg.)	Icing Type†
H	21	20	2.20	2	0, 4	I
I	14	20	1.95	3	0, 4	I
J	–4	20	1.70	3	0	I
K	21	40	0.68	7	0, 4	I
L	14	40	0.52	9	0, 4	I
M	–4	40	0.40	12	0, 4	I

* Calculated using the ice detector simulation method
† I = Intercycle ice case, R = Residual ice case

Several parameters of deicer operation were varied including time to activation, cycle time, total run time, and point of final deicer activation. Time to deicer activation was calculated based upon a simple model of a typical aircraft ice detector. The simple mathematical model of the ice detector gave times to activation based upon the icing conditions for the run. Icing conditions resulting in faster ice accretion rates resulted in shorter times to deicer activation. For the icing conditions in this test, the times to activation varied from two to 34 seconds based on this method (cf. Tables 1 and 2).

Deicer cycle time was set to either a fast cycle rate or a slow cycle rate corresponding to the two settings that are typically available on an airplane equipped with a pneumatic deicer. The two deicer-cycle times, one-minute and three-minutes, were used primarily during the *IM* and *CM* icing conditions, respectively. These corresponded to generally higher and lower rates of ice accretion.

Total run time was determined to be that which had allowed the deicer to reach a "steady state" in terms of amount of ice removed per cycle. In general, the ice accretions reached a "steady state" after two or three deicer cycles. A minimum of four deicer cycles were used to ensure ice accretion "steady state" was reached. For the three-minute cycles used in the *CM* cases, this resulted in a total run time of twelve minutes, not including time to activation. For the one-minute cycles used in the IM cases, total run time was three minutes. The point of final deicer activation refers to the type of ice desired at the end of the run, either residual or intercycle. For the residual ice cases, an additional deicer cycle was performed after the twelve or three minute run time, resulting in a total of five deicer cycles.

For a typical test run, the IWT was brought to the desired air temperature and speed. When the model was at the appropriate temperature, the icing spray was initiated. After the pre-determined time to deicer activation had elapsed, the deicer was cycled and continued to operate at the desired cycle rate while the tunnel's icing spray system operated. When the total run time had elapsed, the icing spray and then the tunnel fan were shut off. For a residual ice run, the deicer was cycled prior to fan shut down. The entire icing run with the deicer operation was recorded on videotape. Tunnel operating conditions were recorded on a personal computer along with the ice thickness measurements from BFGoodrich's OPTRON system. The OPTRON is an optical measurement system that was mounted outside the tunnel.

The model was accessed via a tunnel door from the cold room. Documentation of the ice was made with photos, ice tracings, and ice depth measurements. After photos were taken of the ice on the model, chordwise cuts were made in the ice using an ice knife in three locations along the span of the model. One cut was made at the center of the model span. One was made at the location judged by the researcher to have the most ice and one was at the location judged to have the least ice. Both of these cuts were made within the area covered by the uniform cloud map of the IWT. The profiles of the ice were then traced on cardboard templates in the three locations. Three measurements of ice thickness were taken at each of the cuts. When it was determined that a mold should be taken of an ice shape, a run was repeated after it had been documented. After photos were taken, cuts where then made at only the edges of the uniform cloud. Ice tracings were made at these locations and then the leading edge was removed from the tunnel with the ice intact and mounted on a stand in the cold room. A mold box was then fitted over the ice on the leading edge and the mold material was poured and allowed to cure.

Results and Discussion

Results from the ice accretion tests are presented and discussed in this section. The discussion includes: ice accretion repeatability, a comparison of ice types, the effect of total run time, the effect of angle of attack, a comparison of continuous and intermittent cloud and deicer operation, the effect of cycle time variation, the effect of varying time to deicer activation, and the amount of residual ice remaining on the model after a run. The ice accretions chosen for the molding process and subsequent aerodynamic testing are also presented and discussed.

Even though the ice shedding process from a pneumatic deicer can appear to be random, the pattern of the remaining ice and subsequent ice buildup can be quite repeatable for a given system in repeat icing conditions. Figure 2 shows the intercycle ice tracings from two separate *CM* runs made at the same conditions. While there were a few differences in details, the overall ice thickness distributions and the major features, such as ice limits and upper surface ridge, were similar. This permitted the researchers to make initial runs to evaluate and compare the resulting ice shapes for possible molding, and then make a repeat run to obtain the ice accretion desired for the molding process.

Icing conditions were selected from the FAR Appendix C envelopes that were known to produce glaze, mixed, and rime ice. Tracings from the intercycle ice accretions for each of these conditions with the same deicer operation are shown in Fig. 3. In general, the thickest part of each ice accretion was further forward on the model as the icing conditions

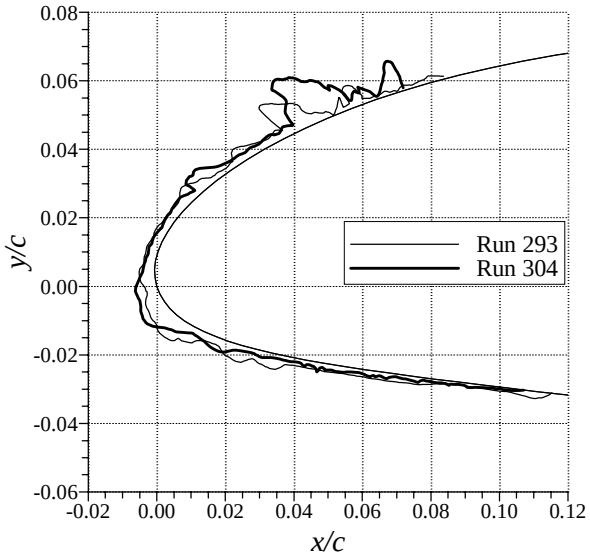

Fig. 2 Comparison of two intercycle ice accretions from two separate (repeat) runs with identical icing and deicer operating conditions; α = 0 deg., icing condition A, Table 1.

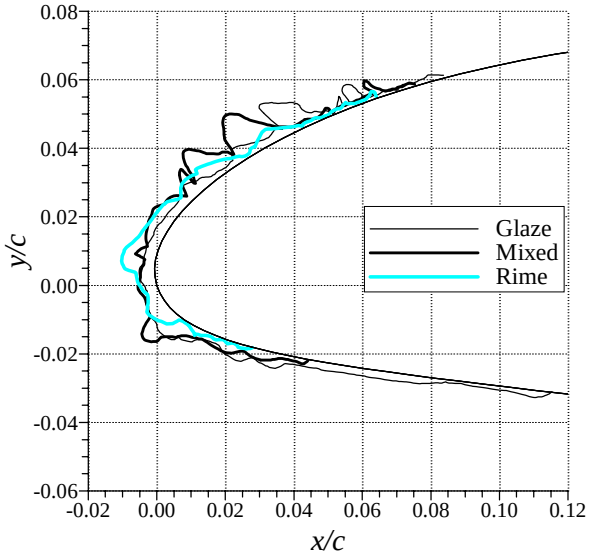

Fig. 3 Comparison of intercycle ice accretions from three different type icing conditions with identical deicer operating conditions; α = 0 deg., icing conditions: Glaze – A, Mixed – B, Rime – C, Table 1.

changed from glaze to mixed to rime with the rime ice having its thickest area at the front of the leading edge. The glaze ice tended to have an ice ridge or some glaze ice feathers furthest aft on the upper surface. The mixed ice also had larger ice buildup on the upper surface aft of the front of the leading edge, but not as far back as the glaze ice. The nature of this ice was different from the glaze, however, being more of a rime feather nature. It also tended to adhere better to the model than the glaze ice.

It was apparent during the course of each run that steady state for the deicer, in terms of amount of ice removed, was consistently being reached after two or three deicer cycles. In order to verify and document this, a *CM* case was run for twice the total run time. The resulting intercycle ice tracing is shown in Fig. 4 along with the tracing from the normal total run time at the same icing and deicer operating conditions. The two tracings are very similar with the exception of a protuberance suggesting a relatively large horn on the upper surface aft of the other major upper surface ice features for the shorter, 12-minute case. This protuberance was actually a freestanding rime feather that happened to form at the location where the centerline tracing was made. It was a single, localized feature not present along the rest of the span. It was not a ridge of ice as might be assumed at first from the tracing. A random occurrence such as this is not unusual during any icing test. The results for this case along with direct observation of the accretion and shedding process during the runs verified that deicer steady state was being achieved during the tests.

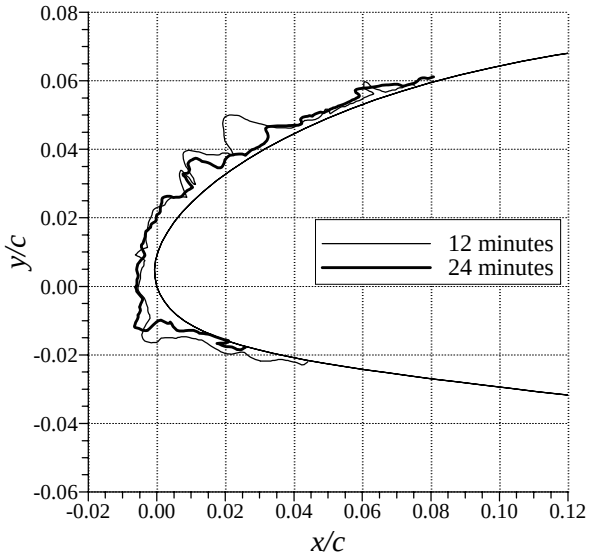

Fig. 4 Effect of total run time on final intercycle ice accretion; α = 0 deg., icing condition B, Table 1.

Figure 5 shows ice accretions from the two angles of attack employed in the tests. As expected, more ice accreted on the upper surface of the model for the zero-degree cases and more accreted on the lower surface for

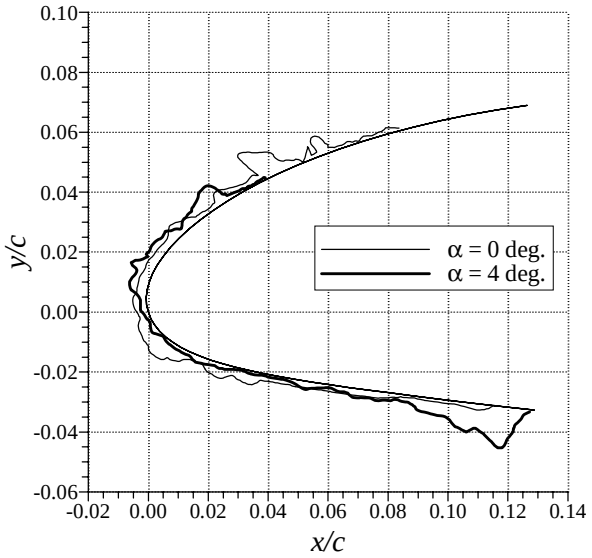

Fig. 5 Effect of model angle of attack on resulting intercycle ice accretions with identical icing and deicer operating conditions; icing condition A, Table 1.

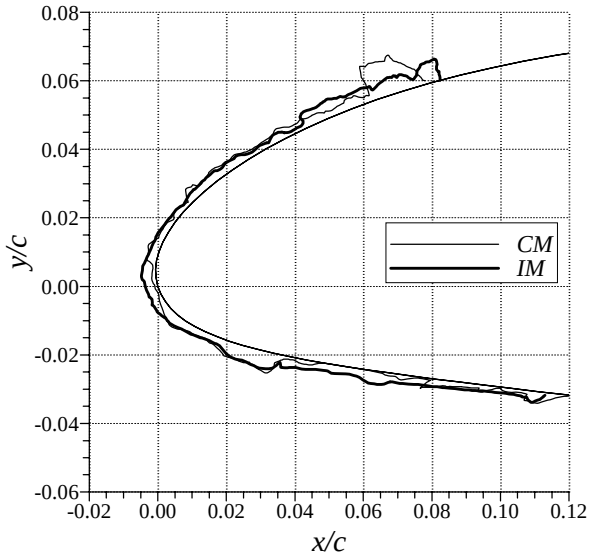

Fig. 6 Comparison of intercycle ice accretions from similar *CM* and *IM* conditions; α = 0 deg., icing conditions: *CM* – D, *IM* – K, Tables 1 and 2.

the four-degree cases. Because upper surface ice accretions are normally considered to have a larger impact on performance, more emphasis was placed on the zero-degree angle of attack cases.

FAR Appendix C intermittent maximum icing conditions result in higher ice accretion rates, but shorter exposure times than continuous maximum icing conditions. Typical flight operating procedures call for shorter times between deicer inflations in *IM* conditions. For these tests, the shorter deicer cycle times, or times between inflations, usually resulted in less severe ice accretions. Figure 6 shows ice tracings from similar *IM* and *CM* conditions. While the ice thickness near the front of the leading edge was about the same even though the ice accretion time was much less for the *IM* case (1 minute vs. 3 minutes), a ridge of ice formed on the upper surface in the *CM* case which was not present in the *IM* case. The non-dimensional measured ice thickness varied from k/c = 0.0131 on the upper surface to k/c = 0.0024 at the stagnation region to k/c = 0.0061 on the lower surface for the *CM* case. For the *IM* case, these measurements were k/c = 0.0068, 0.0049, and 0.0051, respectively.

Cycle time was also investigated for two of the *CM* cases. For most of the *CM* cases, the cycle time was three minutes. However, two *CM* cases were run where the all conditions were the same except the cycle time was set at one minute. Figure 7 shows the intercycle ice tracings for one of these cases. The non-dimensional ice thickness measurements for the three-minute cycle case were k/c = 0.0138, 0.0056, and 0.0127 for the upper surface, stagnation, and lower surface regions, respectively. For the one-minute cycle case, these measurements were 0.0044, 0.0037, and 0.0013. It is evident that the one-minute deicer cycle time was more effective at removing the ice than the three-minute cycle time. This was the result for both of the deicer cycle time variation cases.

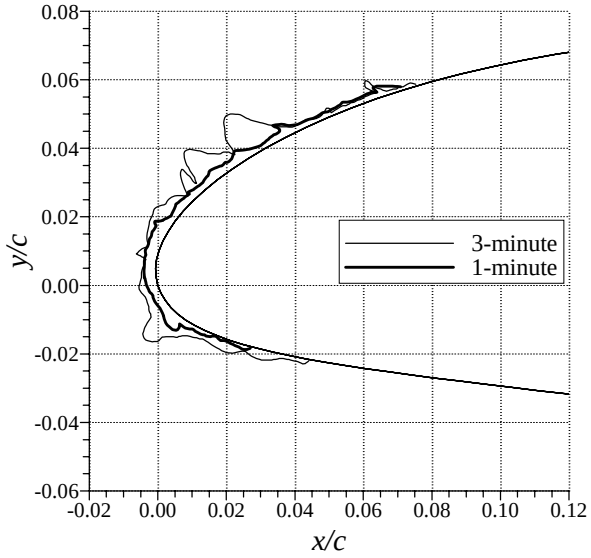

Fig. 7 Effect of deicer cycle time on resulting intercycle ice accretion with identical icing conditions; α = 0 deg., icing condition B, Table 1.

The effect of varying the time to deicer activation was investigated for one icing condition. The baseline activation time was 11 seconds, determined using the ice detector simulation method. Two cases were run using arbitrarily selected times to activation of 30 seconds and two minutes. In addition, a fourth case was run where the deicer was activated when one-quarter of an inch of ice had accreted on the leading edge of the model. This case simulated a commonly used pilot's "rule of thumb" which states that the deicer should not be activated until one-quarter of an inch of ice has accumulated on the deicer. The leading edge ice thickness was measured in real time during the icing tests using the BFGoodrich OPTRON system. These methods all were employed in separate runs at the otherwise same conditions. The resulting ice tracings are shown in Fig. 8. The four tracings are similar with the exception of the upper surface protuberances aft of the other major ice features for both the ice detector simulation case and the two-minute time to activation case. These protuberances suggested that a relatively large horn existed on the upper surface for each of these cases. Again, similar to the case discussed for total run time, both these protuberances were actually freestanding rime feathers that happened to form at the location where the centerline tracing was made. They were single, localized features not present along the rest of the span. Furthermore, they were not features unique to the ice detector simulation method of activation. None of the times to activation offered an advantage over the others in ice removal effectiveness.

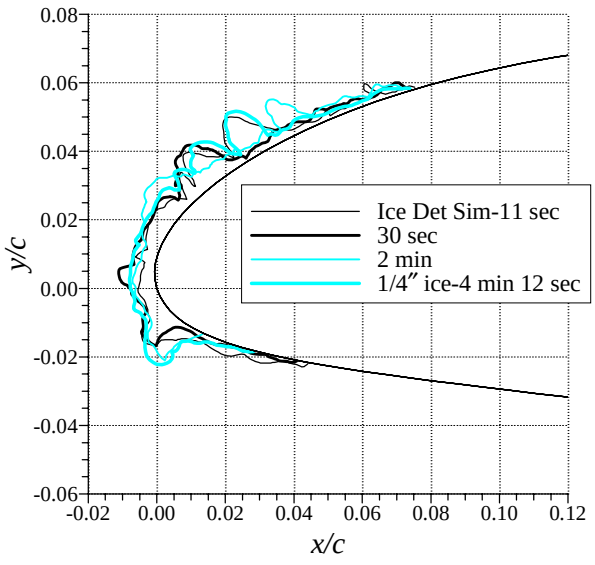

Fig. 8 Effect of deicer activation time on resulting intercycle ice accretion with identical icing conditions; α = 0 deg., icing condition B, Table 1.

Several cases were run to compare residual ice and intercycle ice for the same icing conditions. An example of these results is shown in Fig. 9. As can be seen, the front of the leading edge is clean with only a small, relatively thin amount of ice further aft on the upper and lower surfaces. This was typical of the residual ice cases. Non-dimensional ice thickness measurements for the residual ice case were k/c = 0.0035, 0, and 0.0023 for the upper surface, stagnation, and lower surface regions, respectively. These measurements for the intercycle ice case were k/c = 0.0122, 0.0044, and 0.0073. It was felt that the intercycle ice cases, with ice on the front of the leading edge and protuberances on the upper surface, were more apt to show larger aerodynamic performance degradations.

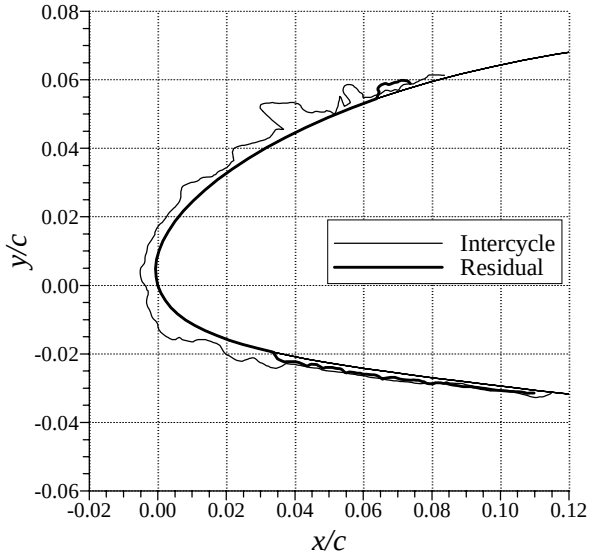

Fig. 9 Comparison of intercycle and residual ice accretions from identical icing conditions and deicer operating conditions; α = 0 deg., icing condition A, Table 1.

Ice Accretions Selected for Molding

The primary objective of the icing tests was to characterize features of residual and intercycle ice and to obtain high fidelity representations of the ice accretions for use in aerodynamic performance tests. For this purpose, molds were made of selected ice accretions. As has been discussed, a number of parameters were examined in determining which ice accretions were molded. Ice accretions that were expected to result in greater performance degradation were more apt to be selected. These were usually accretions with greater amounts ice, particularly on the

upper surface. This tended to occur on the intercycle ice accretions at a zero-degree model angle of attack under continuous maximum mixed and glaze icing conditions with the deicer cycling at three minute intervals. A total of six ice accretions were selected for molds and the test conditions are summarized in Table 3.

The ice shapes selected for aerodynamic testing were from runs 290, 296, 312 and 322. Ice tracings and photos are given for these ice accretions in Figs. 10 through 13. The photographs correspond to the actual run that was molded, except for run 290 in Fig. 10. The photograph in Fig. 10 was from run 292, which was a repeat of run 290. All of the tracings shown in Figs. 10-13 were taken at the model midspan and were also from repeat runs. No tracings were taken at midspan for the mold cases, as this process would have compromised the ice shape fidelity.

Table 3 Summary of intercycle ice accretions that were documented with molds

Ice Shape	Angle of Attack (deg.)	Static Temp. (°F)	Droplet *MVD* (μm)	Cloud *LWC* (g/m^3)	Spray Time (min)	Boot Cycle (min)
290*	0	14	20	0.45	12	3
296*	0	21	20	0.65	12	3
302	4	-4	20	0.25	12	3
312*	0	21	40	0.25	12	3
322*	0	-4	40	0.40	3	1
330	4	14	20	1.95	3	1

* Ice shapes selected for aerodynamic testing

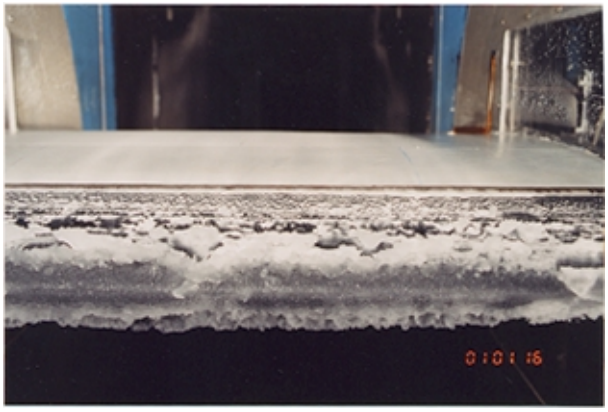

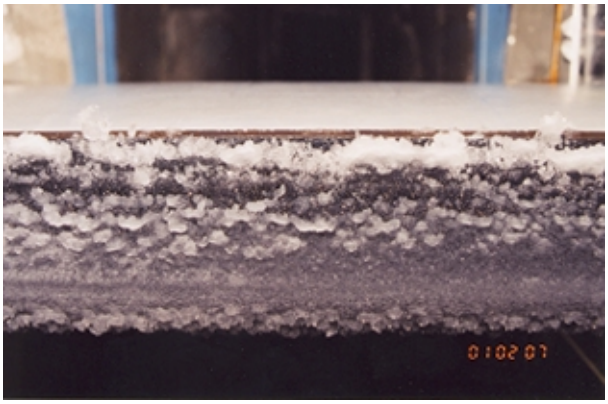

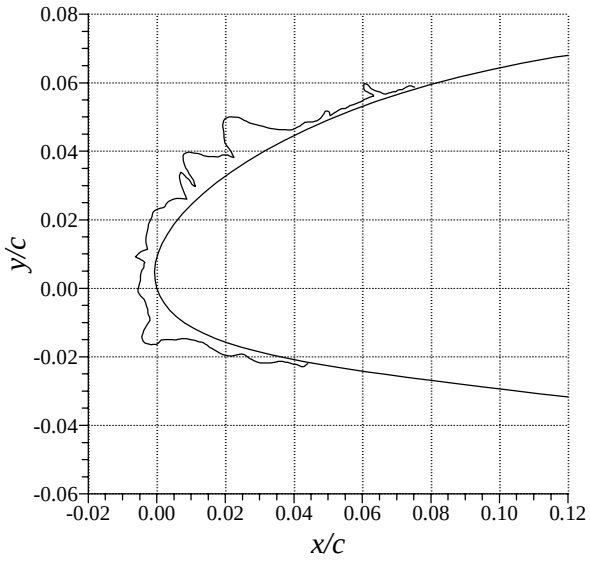

Fig. 10 Photograph and tracing of ice shape 290 (cf. Table 3).

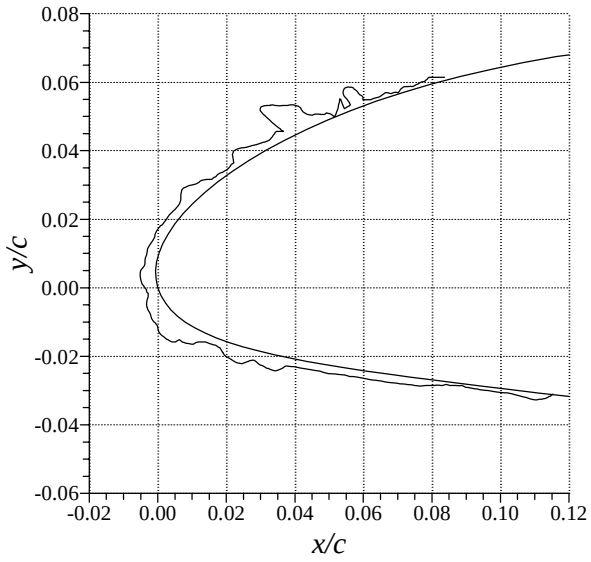

Fig. 11 Photograph and tracing of ice shape 296 (cf. Table 3).

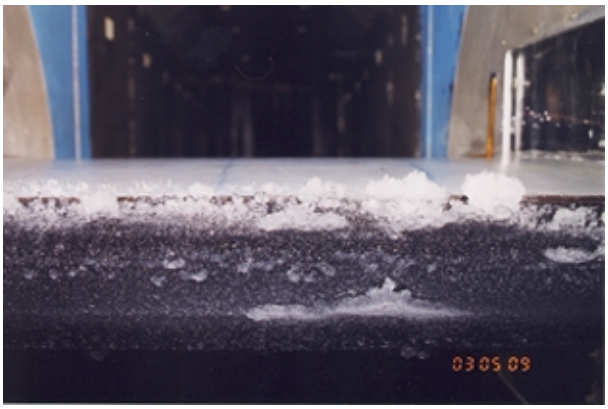

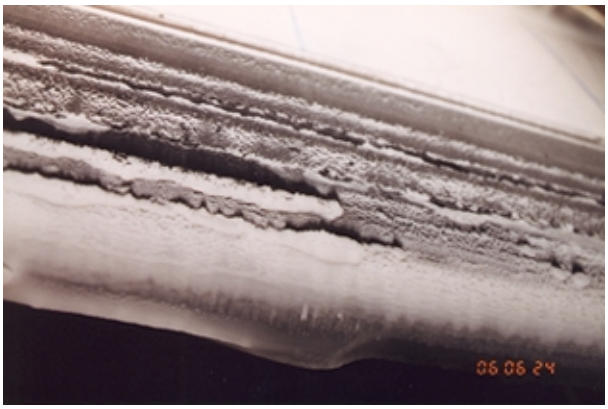

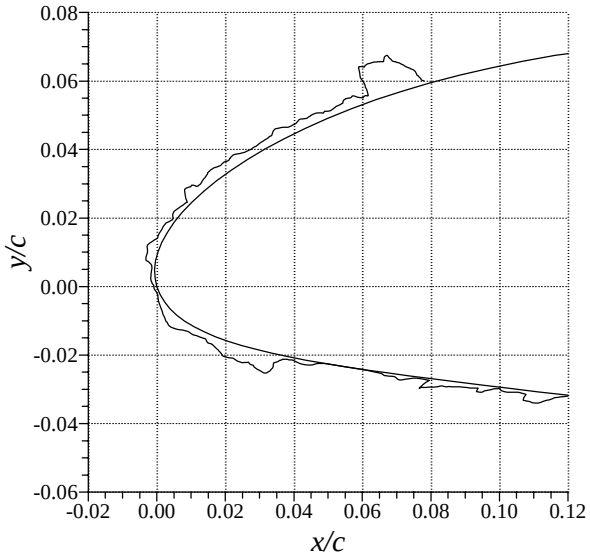

Fig. 12 Photograph and tracing of ice shape 312 (cf. Table 3).

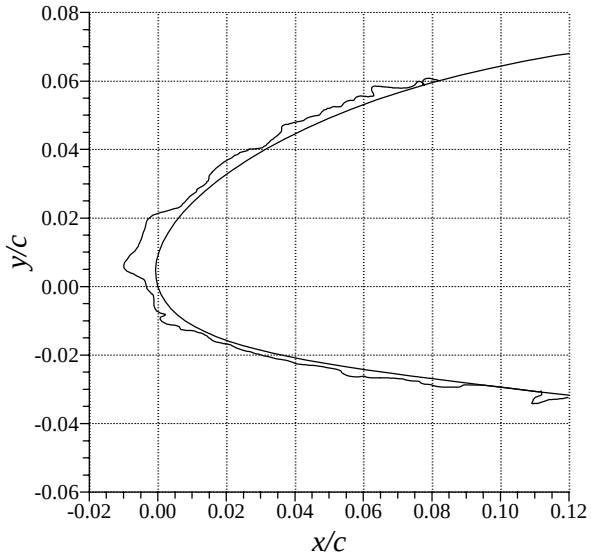

Fig. 13 Photograph and tracing of ice shape 322 (cf. Table 3).

Constraints on time and resources did not allow for testing of all six of the cases shown in Table 3. However, the four ice shapes that were selected for aerodynamic testing provided a reasonable variation in cloud conditions and ice shape type. For example, ice shape 290 (cf. Fig. 10) represents a mixed shape for a continuous maximum case. Ice shapes 296 and 312 (cf. Figs. 11 and 12) are both glaze-type shapes, but the ridge-like features on the upper surface are quite different. This was most likely caused by the difference in droplet *MVD*, which was 20 μm for ice shape 296 and 40 μm for ice shape 312. Finally, ice shape 322 (cf. Fig. 13) represents both rime ice and intermittent maximum cases.

AERODYNAMIC TESTING

Experimental Arrangement

All aerodynamic testing was carried out at NASA Langley, using the Low-Turbulence Pressure Tunnel (LTPT). The LTPT, shown schematically in Fig. 14, is a closed-return wind-tunnel that is principally used for two-dimensional airfoil testing and is described in detail in references 10 and 11. It can be operated at stagnation pressures from near vacuum to 147 psia (except 15 to 20 psia) and over a Mach number range of 0.05 to 0.40. The maximum Reynolds number is dependent upon Mach number. For example, the maximum Reynolds number per foot is 15×10^6 at a Mach number of 0.22. A heat exchanger and nine turbulence reduction screens are located in the inlet settling chamber. The contraction ratio is 17.6:1 and

the test section dimensions are 36-inches wide by 90-inches high by 90-inches long. The tunnel was designed for two-dimensional airfoil testing with model chord lengths up to 36-inches.[10] The free-stream turbulence levels are generally less than 0.1% for all operating conditions.[11] Given these specifications, the LTPT is capable of simulating near-flight conditions for two-dimensional airfoils models.

The 36-inch chord NACA 23012 airfoil model was supported horizontally across the width of the test-section between two 34.5-inch diameter circular endplates. The endplates are flush with the sidewalls and rotate for angle of attack adjustment. They also contained a section of porous plate for sidewall boundary-layer control. This sidewall venting system was originally developed for testing high-lift airfoil configurations and a detailed description is given by Pascal et al.[12] During this study some runs were performed with and without sidewall venting and there was very little difference in the results. All of the data presented here were acquired with sidewall venting, except at $Re = 2.0\times10^6$ as noted below.

The NACA 23012 airfoil model was CNC machined from solid aluminum and had recessed openings for pressure instrumentation. The model was designed and built with a removable leading edge. There was a single baseline, or clean leading edge and an alternate leading edge. The ice-shape castings were mounted to the alternate leading edge. This method simulated the actual ice shape with very high fidelity. In addition, an "instrumentation slice" was installed near the model midspan. The "instrumentation slice" was cut out of stainless steel to match the ice-shape cross-section and had pressure taps distributed around the ice-shape contour. This allowed for a good approximate measurement of the pressure distribution around the ice shape and also provided pressures for determination of the lift and pitching-moment coefficients. The baseline model had 67 static pressure orifices along the main chordwise row and 17 orifices in a spanwise row located at $x/c = 0.70$ on the upper surface. The photograph in Fig. 15 shows the model mounted in the test section, with ice shape and pressure instrumentation slice attached to the airfoil leading edge.

The LTPT was equipped with a three-component force balance, however, it was designed for operation with high-lift systems and for higher dynamic pressures than were run in this experiment. Therefore, the data from the force balance was deemed unreliable except at the higher dynamic pressures and the lift and pitching moment data were generally obtained from the integration of surface static pressures. These data were compared to the force-balance data for large values of dynamic pressure and excellent agreement was observed for both clean and iced configurations. Therefore, no force-balance data were presented here. The pitching-moment coefficient reported here was determined for the quarter-chord location. Drag coefficients were calculated from wake pressures measured with a wake rake using the standard moment-deficit method. One-degree angle of attack increments were used for data collection, except for the wake drag, which was acquired in two-degree increments. Corrections to the integrated performance coefficients accounting for solid and wake blockage and streamline curvature were applied to the data during post-processing using the methods of Allen and Vincenti.[13]

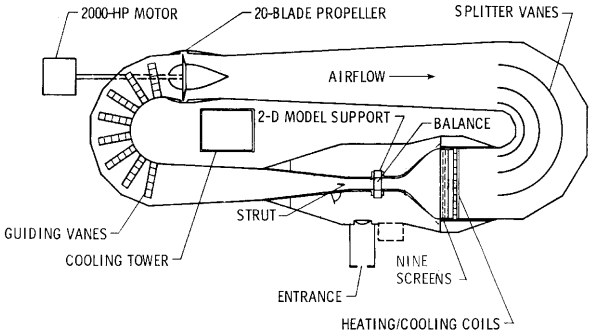

Fig. 14 Schematic drawing of NASA Langley Low-Turbulence Pressure Tunnel (LTPT), after Ref. 18.

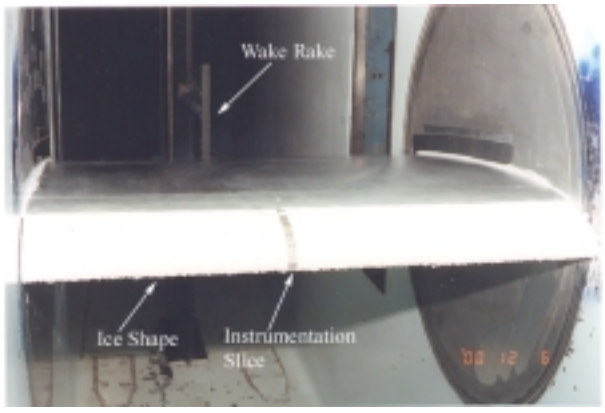

Fig. 15 Photograph of NACA 23012 airfoil model with ice shape in the LTPT test section.

The test matrix was selected to yield a broad range of Reynolds and Mach numbers with the high end being applicable to turbopropeller and piston-engine aircraft as constrained by the limitations of the facility. Table 4 summarizes these conditions for both the clean and iced airfoil configurations. All of the conditions having a Reynolds number of 3.5×10^6 or higher had stagnation pressures above atmosphere, from approximately 20 to 60 psia. Some runs were performed at $Re = 2.0\times10^6$ at and below atmospheric pressure for nominal Mach numbers of 0.095 and 0.21. No sidewall boundary-layer control was available for runs at or below atmospheric pressure. The test matrix was designed to isolate the effects of Reynolds and Mach number. Therefore, there is a Reynolds number variation from 3.5×10^6 to 10.5×10^6 at a fixed Mach number of 0.12. Likewise there is a Mach number variation from 0.12 to 0.28 at constant Reynolds numbers of 7.5×10^6 and 10.5×10^6. In addition to the four ice-shapes selected for testing, some standard roughness was also run for comparison. This standard roughness was 40-grit and 80-grit paper-backed garnet sandpaper that covered the leading edge from $x/c = 0.10$ on the upper surface to $x/c = 0.07$ on the lower surface. A small slit in the sandpaper was made to expose the pressure orifices on the leading edge. The overall heights (including the paper substrate) were measured directly with calipers and were 0.044 inches ($k/c = 0.0012$) for the 40-grit sandpaper and 0.022 inches ($k/c = 0.0006$) for the 80-grit sandpaper. Additionally, this was attached to the model surface with 0.003-inch thick double-backed tape. As with most coarse sandpaper of this type, the paper backing was thick relative to the size of the roughness itself. The nominal size of commercial carborundum is approximately 0.0205 and 0.0083 inches for 40 and 80-grit, respectively.[14]

Table 4 Aerodynamic performance test matrix

Reynolds Number	Mach Number 0.095	0.12	0.21	0.28
2.0×10^6	Clean, Iced		Clean	
3.5×10^6		Clean, Iced		
7.5×10^6		Clean, Iced	Clean, Iced	Clean, Iced
10.5×10^6		Clean, Iced		Clean, Iced

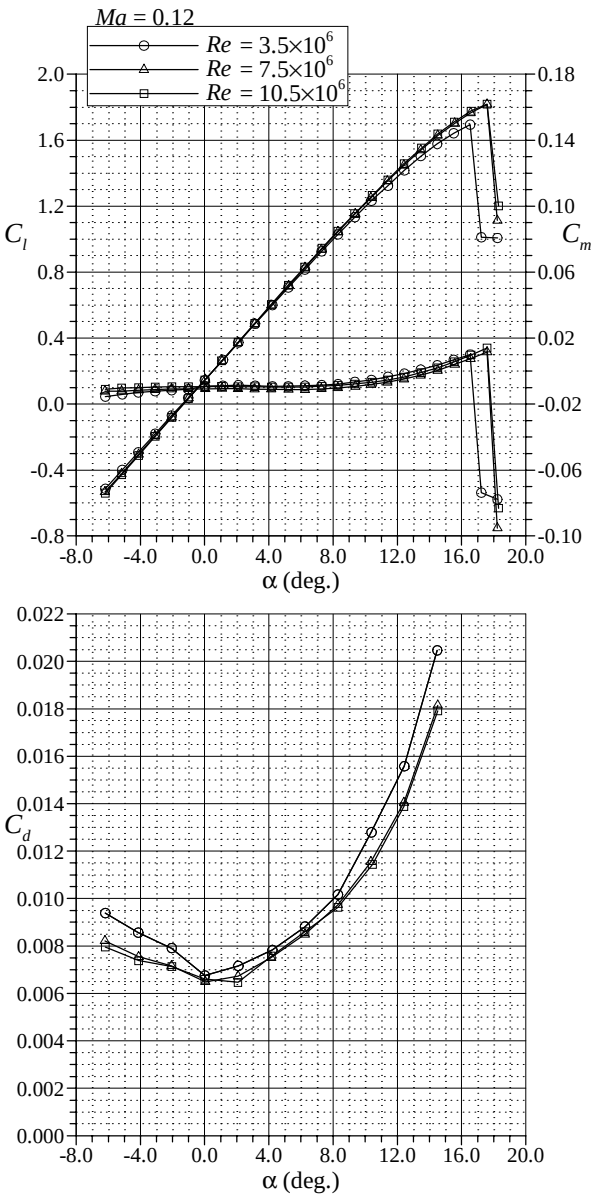

Fig. 16 Effect of Reynolds number at constant Mach number on the performance of the clean NACA 23012 airfoil.

Results and Discussion

Clean Airfoil Configuration

Overall, the clean airfoil results followed classic airfoil behavior and compared favorably with historical data and computational results. Figure 16 shows the effect of Reynolds number at constant Mach number on the performance coefficients. The maximum lift coefficient increased by approximately 0.1 from $Re = 3.5\times10^6$ to $Re = 7.5\times10^6$. Predictable results were also observed in the drag data where the drag coefficients tended to decrease with increasing Reynolds number from $Re = 3.5\times10^6$ to $Re = 7.5\times10^6$. The effect of Mach number at constant Reynolds number is illustrated in Fig. 17. Again, classic airfoil behavior was observed in the performance coefficients. The lift-curve slope increased with Mach number, but $C_{l,max}$ decreased about 0.05 from $Ma = 0.12$ to $Ma = 0.28$. The stalling angle of attack was also reduced about one degree. The difference in stall parameters was more pronounced at $Re = 10.5\times10^6$, where $C_{l,max}$ was reduced by 0.1 and

α_{stall} was reduced by two degrees as the Mach number was increased from 0.12 to 0.28. Classic Mach number effects were observed in the drag and pitching moment data as well. There was a significant increase in drag at low angles of attack from Ma = 0.21 to 0.28. The increasing $C_{l,\alpha}$ noted above occurred along with an attendant increase in C_d. The variation in pitching moment indicates that the airfoil became more front loaded, for higher angles of attack, as the Mach number increased. The clean airfoil data acquired at Re = 2.0×10^6 showed no dependence on Mach number over the range that was tested. As illustrated in Fig. 18, there is very little difference in the performance coefficients for a greater than two-fold increase in Mach number. Conversely, the increase in Reynolds number caused the $C_{l,max}$ to increase about 0.2.

The independent effects of Reynolds and Mach numbers on the performance coefficients must also be considered when comparing data from different facilities or with historical data. For example, the NACA 23012 data in Abbot and von Doenhoff[15] were for large Reynolds number variations (from 3.0×10^6 to 9.0×10^6), but the Mach number variation was not reported. The authors do say that the Mach numbers

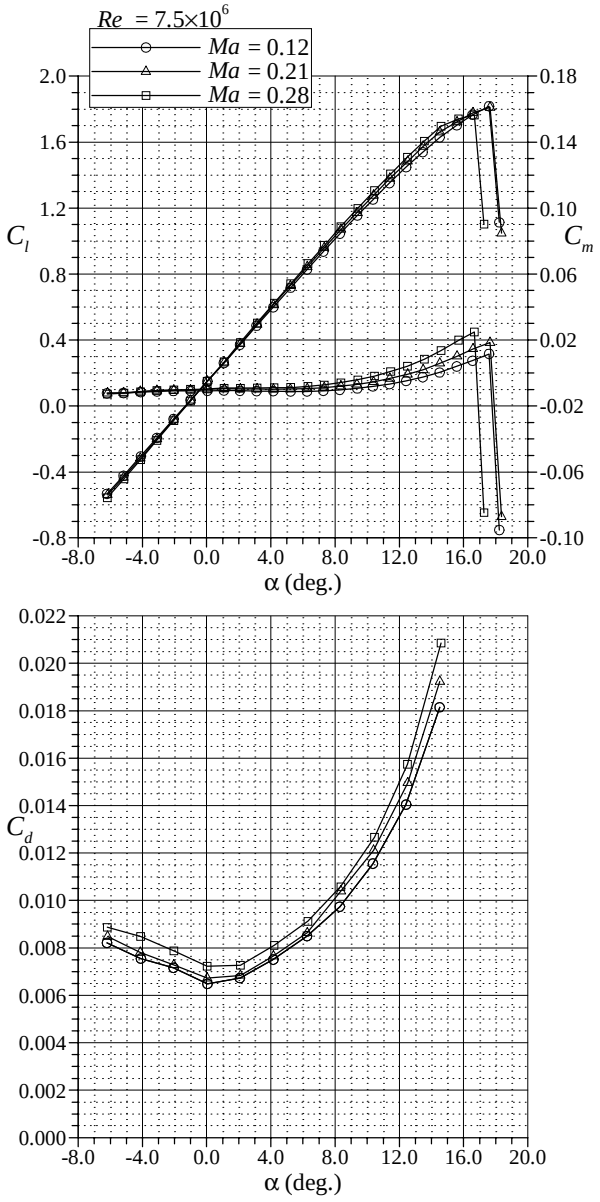

Fig. 17 Effect of Mach number at constant Reynolds number on the performance of the clean NACA 23012 airfoil.

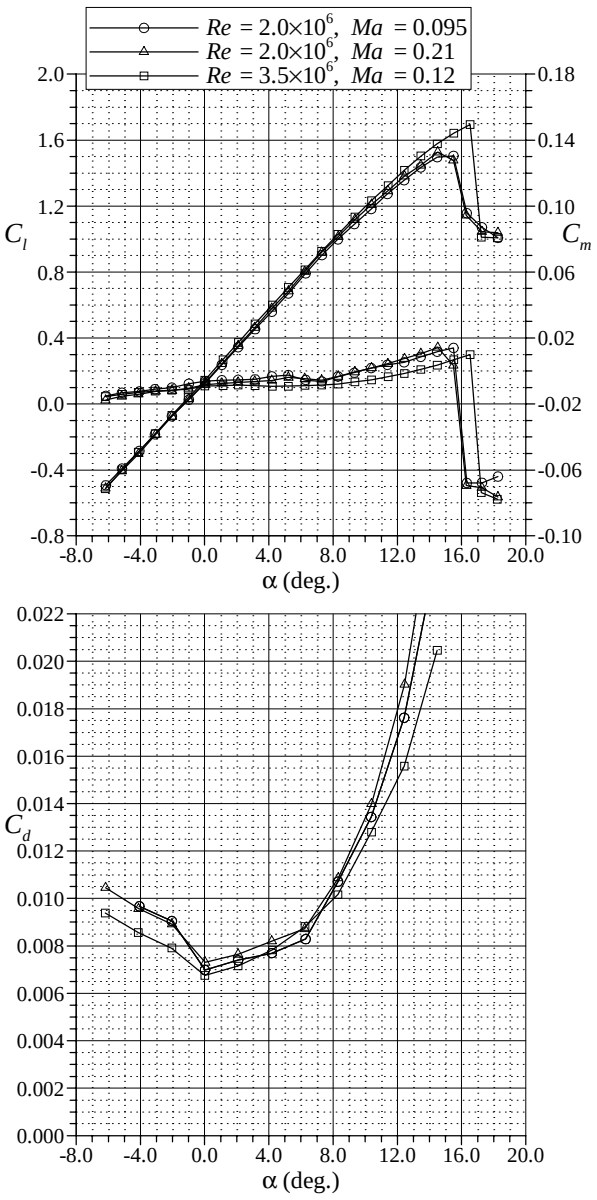

Fig. 18 Effect of Mach and Reynolds number on the performance of the clean NACA 23012 airfoil.

were "less than about 0.17." Despite the Mach number vagueness, the Abbott and von Doenhoff data are suitable for comparison to the present data. Before this is discussed, it is worthwhile to note other procedural details about the historical data. Coincidentally, the data were acquired in the LTPT, although it was then known as the "Two-dimensional Pressure Tunnel." The NACA 23012 airfoil model had a 24-inch chord and no sidewall boundary-layer control existed at the time. The lift coefficients were determined "by integration of pressures representing the reaction on the floor and ceiling of the tunnel." That is, no airfoil surface pressure were available as in the present data. The pitching moment data were "measured directly by a balance." The drag coefficients were determined from wake surveys. It is reasonable to assume that the data were corrected for solid-boundary effects as discussed by von Doenhoff and Abbott.[10]

The present data are co-plotted with data extracted from Abbott and von Doenhoff[15] for the freestream conditions shown in Fig. 19. There is excellent agreement in the lift coefficient data, with the $C_{l,max}$ values being nearly identical. The agreement in the pitching moment coefficients is surprisingly good, given that there were two significant factors affecting the historical data. First, extracting C_m data from the plots in Abbott and von Doenhoff[15] was difficult because of the poor resolution in the scale divisions. Secondly, it is reasonable to assume that the balance was designed for the large pitching moments associated with multi-element airfoils operating at the high dynamic pressures available for the facility. Therefore, the relatively low pitching moments for the single-element NACA 23012 airfoil may have been difficult to resolve accurately. The drag coefficients for the historical data were significantly lower than for the present data. This may have been caused by the model design and is addressed below. Comparisons between the present and historical data for the lower Reynolds numbers (3.0×10^6 and 6.0×10^6) showed similar results. Lift coefficient data matched very well in the linear range. The present data yielded slightly higher maximum lift values, on the order of 0.1 in C_l, but the stalling angles of attack were nearly identical. Overall, the agreement in the lift data illustrated the reasonable quality of the Abbott and von Doenhoff[15] data, especially given the obvious technical limitations at the time.

The clean airfoil data were also compared to computational results generated using XFOIL,[16] which is an airfoil analysis code that couples a panel method flowfield solver to an integral boundary-layer formulation. Several cases were run to compare with the experimental data and these results are highlighted

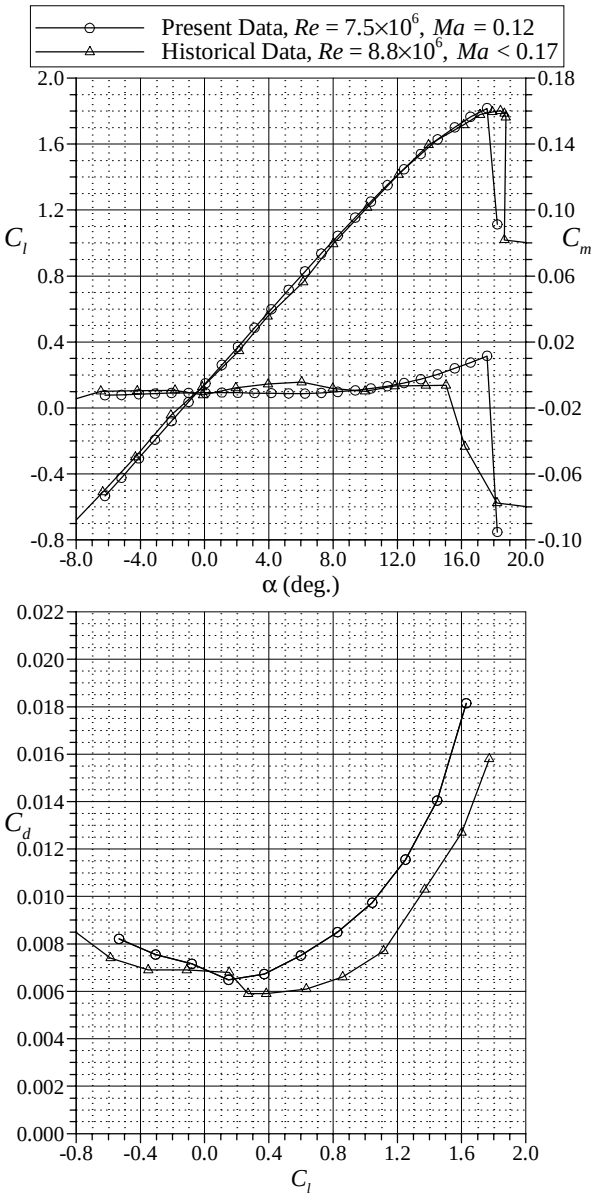

Fig. 19 Comparison of clean NACA 23012 airfoil performance data from the present study with historical data from Abbott and von Doenhoff.[15]

here. Figure 20 shows the present data compared to XFOIL results with free and fixed boundary-layer transition. The lift coefficient plot shows that the XFOIL results agreed very well with the experimental data up to about 9 deg. angle of attack. At this point and for higher angles, XFOIL over-predicted the lift coefficient. This is a common feature of XFOIL results, in the authors' experience. The pitching moment data tended to agree fairly well over the entire angle of attack range shown. Finally, in the drag data, the XFOIL drag values for the free boundary-layer transition case were much lower than for the

experimental data. In fact, the minimum XFOIL drag values were lower than the Abbott and von Doenhoff[15] data shown previously in Fig. 19. This under-prediction of minimum drag is also a common characteristic of XFOIL results in the authors' experience.

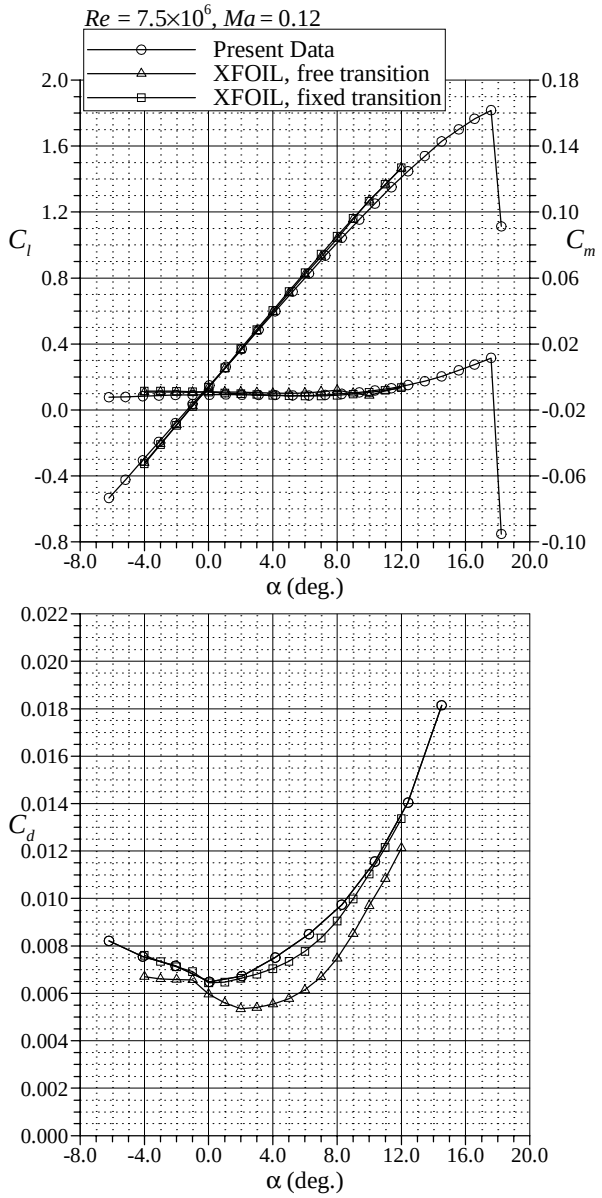

Fig. 20 Comparison of clean NACA 23012 airfoil performance from the present study with XFOIL results for free and fixed transition.

The XFOIL results for the fixed transition case show that higher drag values in the present data may have been caused by the removable leading edge. Unlike the completely smooth Abbott and von Doenhoff[15] model, the present model had a removable leading edge and pressure orifices. The removable leading edge joined the main body at x/c = 0.21 on the upper and lower surface. Ideally this spanwise-running seam would have been smooth so as not to cause any flow disturbance. In practice, this was difficult to achieve and it is possible that there was enough misalignment to cause boundary-layer transition at this location. The XFOIL results for free transition showed that boundary-layer transition on the upper surface occurred downstream of x/c = 0.21 for angles of attack less than two degrees. Boundary-layer transition occurred on the lower surface downstream of x/c = 0.21 for angles of attack greater than −1 deg. Using this information, the "fixed transition" calculation was performed with the transition location fixed at the seam (at x/c = 0.21) on the upper surface for angles of attack less than two degrees and on the lower surface for angles of attack greater than -1 deg. As shown in Fig. 20, this had virtually no effect on the lift and pitching moment results, but increased the drag substantially, such that it agreed much better with the present data. While this calculation is by no means conclusive, it does show that the removable leading edge (plus pressure taps, etc.) may play a role in the departure of drag values from the Abbott and von Doenhoff[15] data. This sort of trade-off was expected, given the necessary compromises in model quality required to perform the ice shape testing.

The independent effects of Reynolds and Mach numbers on the clean airfoil performance described earlier is representative of classic airfoil behavior and is also consistent with previous LTPT results. For example, Ladson[17] analyzed data from the testing of a NACA 0012 airfoil having a 24-inch chord, acquired with solid sidewalls (no sidewall boundary-layer control) over a large matrix of Reynolds and Mach numbers. The NACA 0012 and 23012 airfoils are very similar in that they have identical thickness distributions.[15] The major difference is that the latter is cambered while the former is symmetric. The similarity in the variation of maximum lift with Reynolds number at constant Mach number is shown in Fig. 21. The NACA 23012 camber led to higher absolute values of the $C_{l,max}$, but the Reynolds number behavior was nearly identical to the NACA 0012 $C_{l,max}$ data. Note that the present data at $Re = 2.0\times10^6$ was for Ma = 0.095. This was appropriate since there was little change in $C_{l,max}$ from Ma = 0.095 to 0.21, as shown in Fig. 18. The effect of Mach number on $C_{l,max}$ at constant Reynolds number is shown in Fig. 22. The present data do not show nearly as strong Mach number dependence as in the Ladson data.

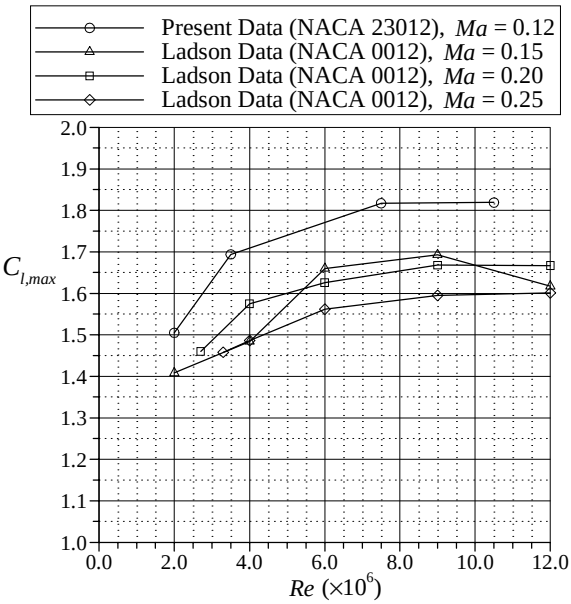

Fig. 21 Comparison of maximum lift Reynolds number dependence for the present study with the data of Ladson.[17] (Note that the present data at *Re* = 2.0×10^6 was at *Ma* = 0.095)

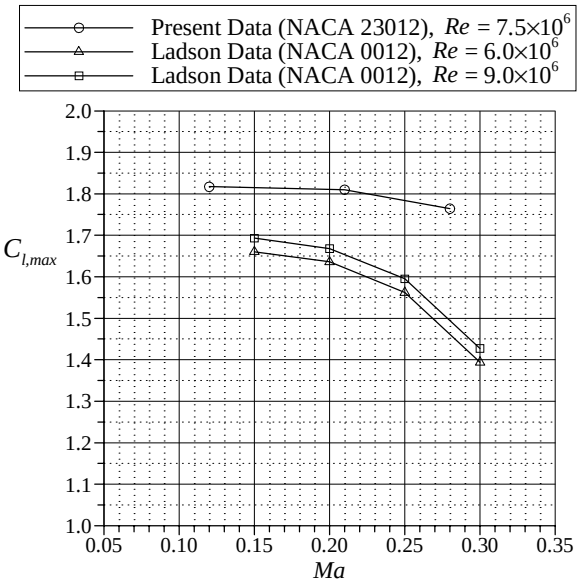

Fig. 22 Comparison of maximum lift Mach number dependence for the present study with the data of Ladson.[17]

Iced-Airfoil Configurations

The performance penalties due to the inter-cycle ice shapes were found to be very severe. This is illustrated in Fig. 23 for $Re = 7.5\times10^6$ and $Ma = 0.21$. Three of the four ice-shape castings mounted to the airfoil leading edge (290, 296 and 312) caused nearly the same performance degradation, despite their differences in geometry. The maximum lift coefficient for these shapes was in the range of 0.65 to 0.75. This represents a 60% reduction from the clean value of 1.8. The stalling angle was reduced from 17.5 deg. to about 8.5 deg. Furthermore, significant degradations in the iced-airfoil lift coefficients was apparent for angles of attack greater than four degrees. Ice shape 322 was formed from one-minute boot cycles in rime-ice conditions and it resulted in a slightly lower maximum lift penalty of about 50%. All of the ice-shape castings caused a significant change in the airfoil pitching moment. In the clean case, the pitching moment was nearly constant over the linear-lift range. With the ice

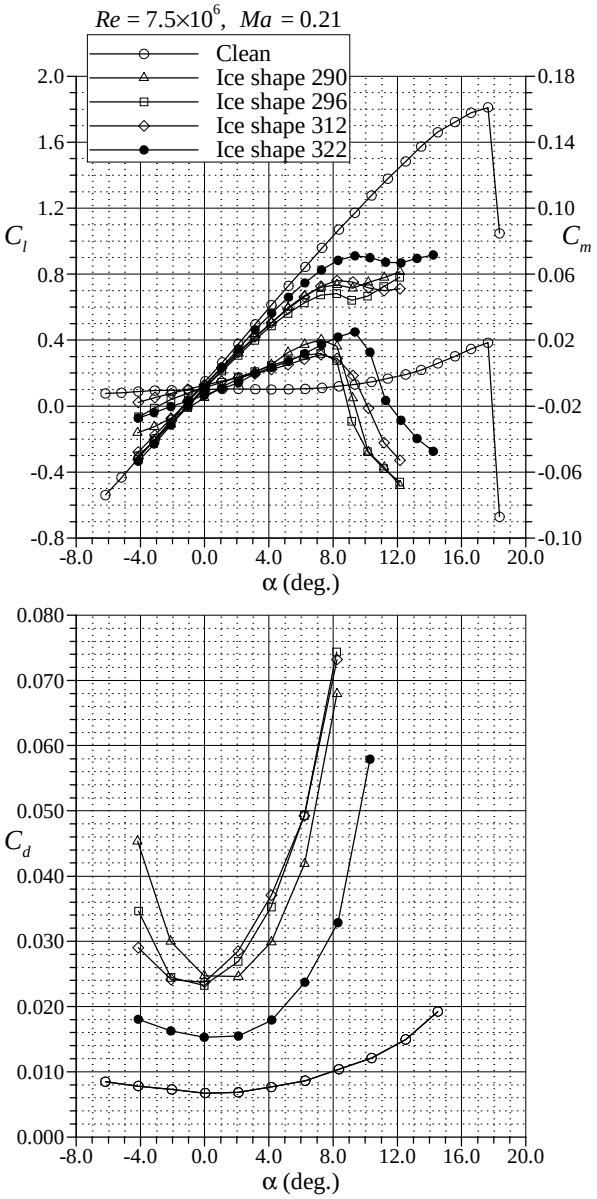

Fig. 23 Effect of intercycle ice accretion simulations on the performance of the NACA 23012 airfoil.

shapes attached to the airfoil, the pitching moment had a strong angle of attack dependence. The drag data showed at least a three-fold increase in the minimum C_d for three of the four shapes. The ice shape 322 case had a smaller increase in drag, probably because the shape was smaller and smoother.

The NACA 23012 airfoil section was also tested with 40 and 80-grit sandpaper applied to the leading edge. This test was performed in order to compare the performance degradation due to a standard, or uniformly distributed, roughness to the performance degradation due to the ice-accretion castings. The use of sandpaper as "standard roughness" is advantageous because it is easily duplicated for testing in other facilities or in flight. Figure 24 shows that the sandpaper performance penalties were about half that of the ice-shape castings. The average reduction in $C_{l,max}$ was about 33% with α_{stall} being reduced from 17.5 deg down to about 12 deg. The drag values for the airfoil with sandpaper were generally closer to the clean case than with the ice-shape castings attached. The chief short coming of the sandpaper simulation was that the roughness heights were not close to those of the actual ice accretions. For example, the nominal height (ignoring the larger ridge-like features) of ice shape 290 was k/c = 0.0056, while the 40-grit sandpaper was nearly five times smaller at k/c = 0.0012. Further, the sandpaper simulation did not capture any of the ridge-like features of the intercycle ice accretions. This ice-shape geometry effect is revisited later.

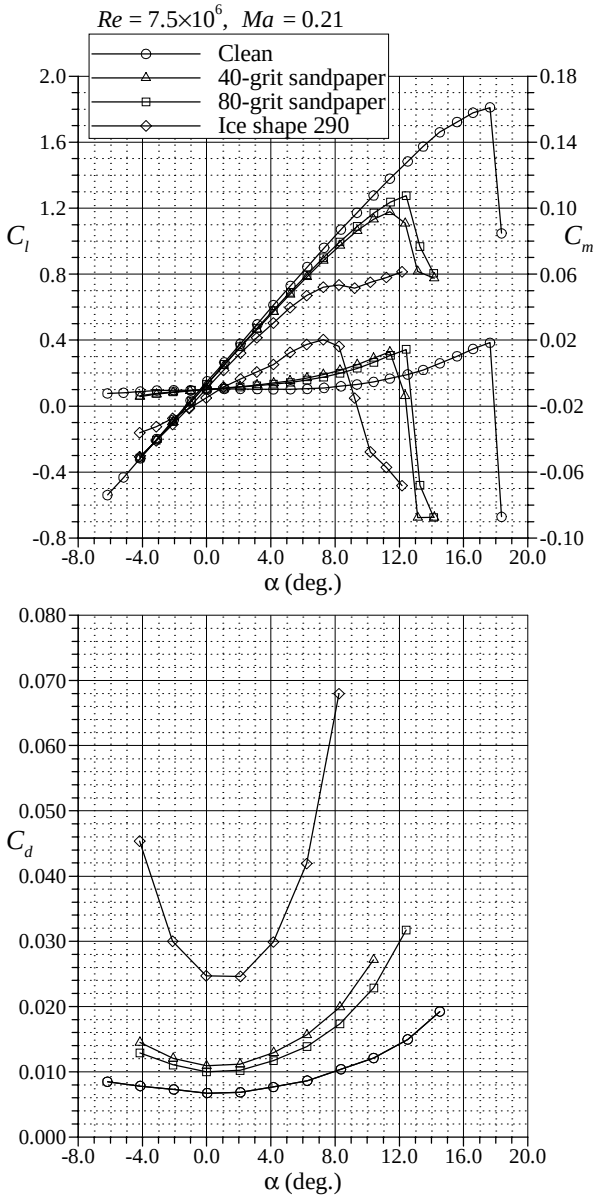

Fig. 24 Effect of 40 and 80-grit sandpaper on the performance of the NACA 23012 airfoil.

Reynolds and Mach Number Effects

The effect of Reynolds and Mach number variation was investigated for all of the ice shapes. An example of these effects is shown in Figs. 25 and 26 for the airfoil with the ice shape 290 casting attached. The lift coefficient data in Fig. 25 show that there was a small increase in $C_{l,\alpha}$ and $C_{l,max}$ from $Re = 2.0\times10^6$ to 3.5×10^6, but there was virtually no change for the higher Reynolds numbers. The drag data exhibited a similar trend where the largest variation occurred from $Re = 2.0\times10^6$ to 3.5×10^6. Figure 26 shows that there was a measurable variation in $C_{l,max}$ with Mach number at constant Reynolds number. The drag coefficients tended to increase slightly with increasing Mach number at higher and lower angles of attack. These trends are similar to the clean case, where $C_{l,max}$ decreased with increasing Mach number and the drag increased. However, these differences were very small relative to the overall performance degradation due to the ice shape.

These Reynolds and Mach number trends were generally observed for all of the iced-airfoil configurations tested. The effect of Reynolds number on the maximum lift coefficient is summarized in Fig. 27. As indicated above, there is only a minor increase (less than 0.05 in C_l) in maximum lift coefficient from $Re = 2.0\times10^6$ to 3.5×10^6, for the ice-shape castings. This increase was more significant (approximately 0.1 in C_l) with sandpaper over the leading edge. Figure 28 illustrates that the slight decrease in $C_{l,max}$ over the Mach number range tested was similar for all of ice-shape castings. The Mach number behavior was different in the case of the sandpaper as the opposite trend is shown for the 80-grit case.

The Reynolds and Mach number trends observed for the iced-airfoil cases are consistent with previous

research performed by others. For example, Morgan et al.[18] carried out iced-airfoil performance measurements on a multi-element super-critical airfoil. A large glaze-ice simulation made of wood was tested as well as simulated frost that consisted of 70-grit roughness. Performance measurements were carried out with all airfoil elements nested (cruise configuration) at a constant Mach number of 0.20 with $Re = 3.0\times10^6$ to 12×10^6. The results showed very minor changes in maximum lift over the entire Reynolds number range for the iced-airfoil cases. In another study, Addy and Chung[19] tested glaze-ice simulations on an NLF-0414 airfoil in the LTPT. The simulations consisted of castings produced from actual ice accretions (similar to the present study) and corresponding two-dimensional (i.e., uniform in the spanwise direction) smoothed shapes produced using rapid-prototyping methods. The ice accretions resulted from a 6-minute and 22.5-minute exposure to the same cloud condition. For three of the four iced-airfoil configurations tested, there was virtually no variation in $C_{l,max}$ for $Re = 4.6\times10^6$ to 10.5×10^6, at a constant Mach number of 0.21. There was a minor increase in $C_{l,max}$ over this Reynolds number range for the 22.5-minute, two-dimensional ice case.

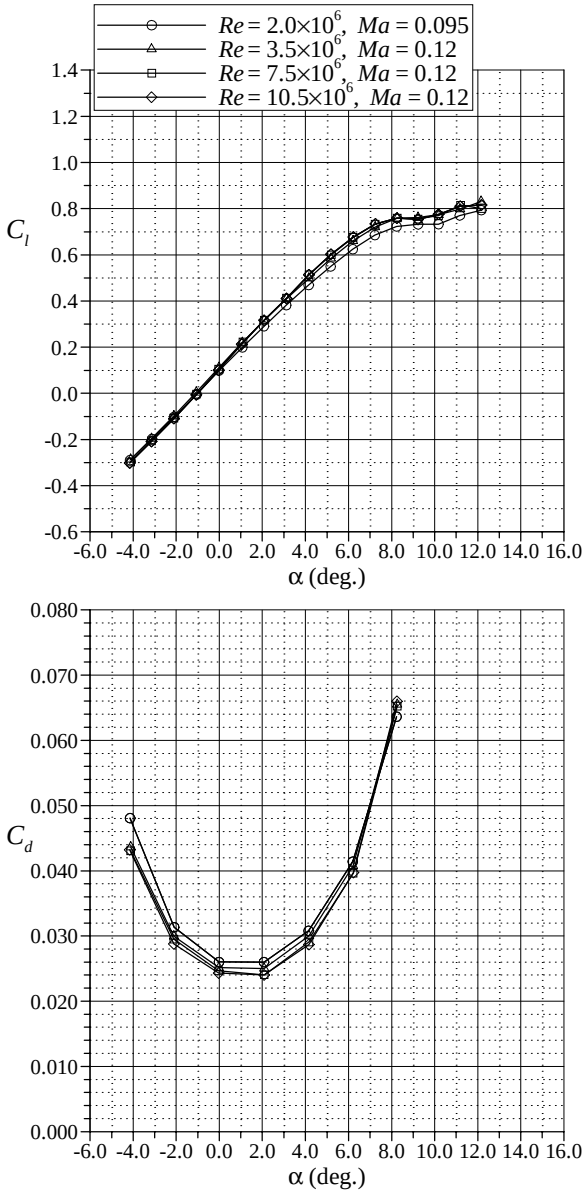

Fig. 25 Effect of Reynolds number on the performance of the NACA 23012 airfoil with ice shape 290.

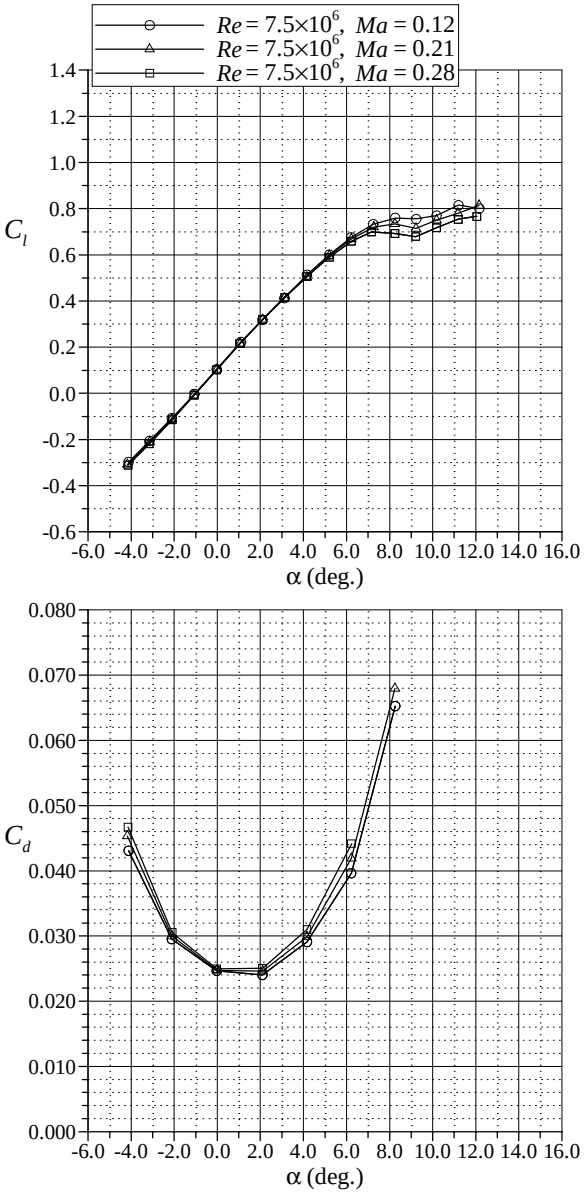

Fig. 26 Effect of Mach number on the performance of the NACA 23012 airfoil with ice shape 290.

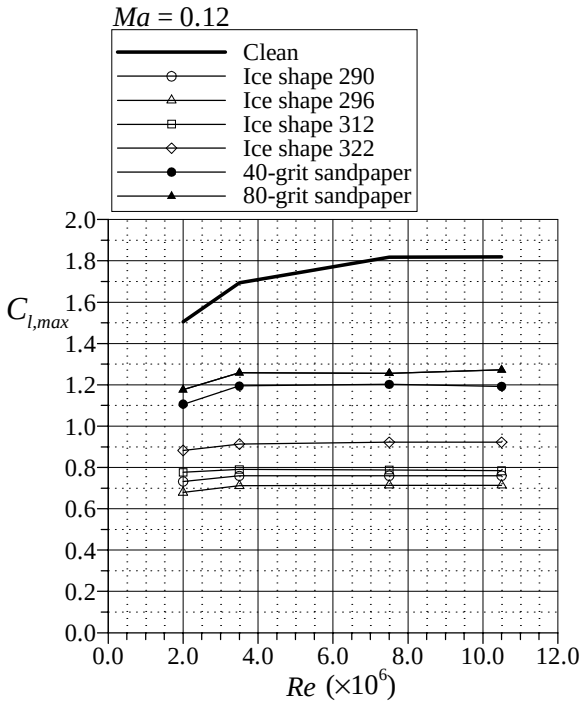

Fig. 27 Effect of Reynolds number on maximum lift for various NACA 23012 airfoil configurations. (Note that data at $Re = 2.0\times10^6$ was at $Ma = 0.095$)

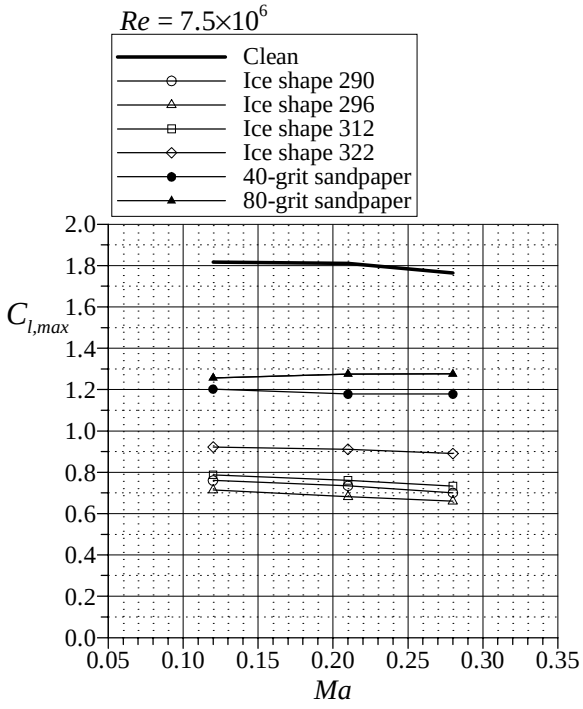

Fig. 28 Effect of Mach number on maximum lift for various NACA 23012 airfoil configurations.

The trends observed in the present and previous data further illustrate that the maximum lift of an airfoil with simulated ice, roughness or other contamination is relatively insensitive to changes in Reynolds number. This is true once the Reynolds number exceeds a critical value that is dependent upon size of the ice accretion or roughness. Lee et al.[1] examined historical roughness data for a NACA 0012 airfoil and suggested that for a typical small-sized ice accretion (k/c = 0.0009) this critical Reynolds number was below 0.1×10^6. The data from this and previous studies shows that the Reynolds number variation in iced-airfoil performance is minor relative to the degradation from the clean values. This implies that iced-airfoil performance measured at lower Reynolds number (say $Re \approx 2.0\times10^6$) is very valuable and may be carefully applied to higher Reynolds numbers cases.

The Mach number effect on the iced-airfoil performance has not received as much attention in previous studies. However, Addy and Chung[19] reported lift-coefficient results for a Mach number variation from 0.12 to 0.29 at $Re = 6.4\times10^6$. There was a slight decrease in $C_{l,max}$ and α_{stall} with increasing Mach number for all of the ice-shape configurations tested. The magnitude of this decrease is very similar to that shown in the present data. However, the conclusion is identical to that for the Reynolds number effect. The dependence of maximum lift on Mach number in the iced-airfoil case is minor relative to the overall performance degradation caused by the ice accretion.

Ice-shape Geometry Effects

The large degradation in the maximum lift coefficient for these ice accretions is likely related to the pressure distribution on the NACA 23012 airfoil. Since the clean airfoil has a large suction peak near the leading edge, the airfoil is more sensitive to protuberances in this region. It is likely that an airfoil with a more gradual pressure recovery would have less severe lift degradation due to a similar ice shape. This idea is explained in more detail by Lee[20] and Lee et al.[1,21] For example, a significant feature of ice shape 296 is the large spanwise ridge located at $x/c \approx 0.04$ (cf. Fig. 11). The effect upon the pressure distribution is illustrated in Fig. 29. The data are for approximately eight degrees angle of attack which corresponded to α_{stall} for the iced-airfoil case. The plot shows how the leading-edge suction pressures were reduced due to the presence of the ice accretion casting. There was also significant deviation of the lower-surface pressure. This behavior is contrasted with the effect of the uniformly distributed roughness shown in Fig. 30. The data are for 11.4 deg. angle of attack, which corresponded to α_{stall} for the airfoil with 40-grit

sandpaper over the leading edge. The pressure distributions show that there was significant deviations only in the region of minimum pressure. As mentioned above, the size of the 40-grit sandpaper tended to be about five times smaller than the typical nominal height of the intercycle accretions. In addition, the sandpaper did not simulate the ridge-like protuberance features of the inter-cycle accretions.

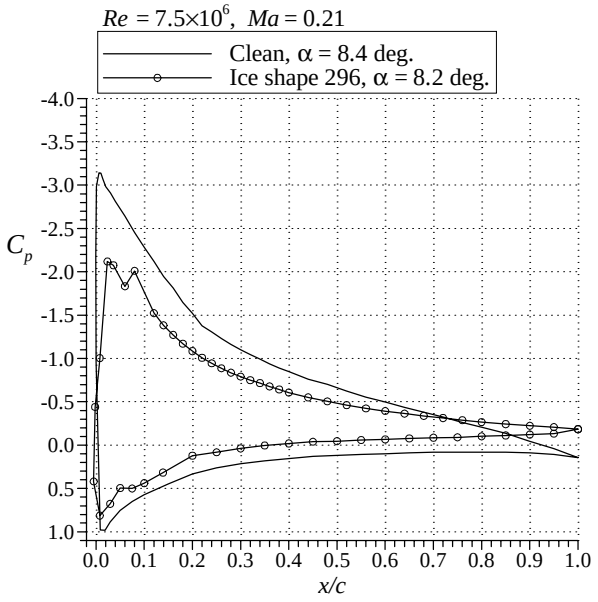

Fig. 29 Comparison of clean and iced NACA 23012 airfoil pressure distributions.

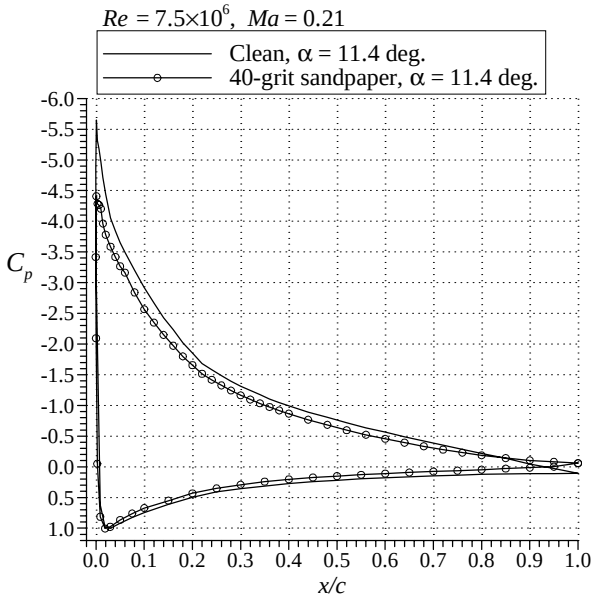

Fig. 30 Comparison of clean NACA 23012 pressure distributions with that having sandpaper over the leading edge.

The effect of spanwise-ridge protuberances on airfoil performance has been investigated by others and some comparison to the present data is warranted. For example, Jacobs[22] parametrically varied the spanwise protuberance height and location on a NACA 0012 airfoil. The data tended to indicate that larger sized protuberances ($k/c > 0.001$) located on the upper surface just aft of the leading edge caused the most significant degradation in maximum lift. Similar results were presented by Lee et al.[1] for tests with a forward-facing quarter-round on a NACA 23012m airfoil. In this case, the quarter-round protuberance caused the most significant decrease in maximum lift when located at $x/c = 0.10$ to 0.15.

The dominant ridge-like features of the intercycle ice shapes was obtained using the digitized ice-shape tracings shown in Figs. 10-13. For example, ice shape 296 had a large ridge-like feature located at approximately $x/c = 0.035$. Using the digitized tracing in Fig. 11, the height of this ridge was determined to be $k/c = 0.0122$. Table 5 summarizes the corresponding features extracted from the other ice shape tracings. The data from the table are plotted along with the aforementioned data of Lee et al.[1] for the NACA 23012m airfoil in Fig. 31. The NACA 23012m is a slightly modified version of the NACA 23012 airfoil used for the present experiments. The plot shows that the $C_{l,max}$ degradation due to the intercycle ice shapes is generally less than for the single quarter-round protuberance. This is true for all of the shapes except 322, which resulted in a lower $C_{l,max}$ than for the corresponding quarter-round case. This probably occurred because the actual ice shape (cf. Fig. 13) wrapped around the leading edge, covering more surface extent than the Lee et al.[1] quarter-round. For the other three shapes, there are two probable reasons why the loss in $C_{l,max}$ is not as large for the intercycle ice accretions. The first reason is that the spanwise ridges are not uniform in the case of the intercycle accretions. This is clearly illustrated in Fig. 12 for ice shape 312, where the ridge is broken in several places along the span. On the other hand, the quarter-round cross-section of Lee et al.[1] was invariant across the span. Correspondingly, Fig. 31 shows the most disagreement in $C_{l,max}$ for this ice shape. Lee[20] investigated the effect of spanwise breaks or gaps for a $k/c = 0.0138$ quarter-round at $x/c = 0.10$. Even relatively small spanwise breaks in the quarter-round caused the $C_{l,max}$ to increase from 0.27 to approximately 0.50. The second reason is that the quarter-round spanwise ridge caused a large separation region in front of the ridge.[20,21] This was different from the intercycle accretions because the spanwise ridges formed aft of an accretion that covered the entire leading-edge region.

This likely reduced the effects of any separated flow region that may have existed immediately upstream of the ridge-like feature. The combined results of this comparison and the uniform roughness testing indicate that any aerodynamic simulation of the intercycle ice accretions should incorporate both the appropriate ice-roughness height and ridge-like features.

Table 5 Summary of ridge-like features from intercycle ice accretions

Ice Shape	Ridge Height (k/c)	Location (x/c)	$C_{l,max}$ *
290	0.0138	0.020	0.734
296	0.0122	0.035	0.682
312	0.0131	0.060	0.761
322	0.0091	0.000	0.911

* For $Re = 7.5\times10^6$, $Ma = 0.21$

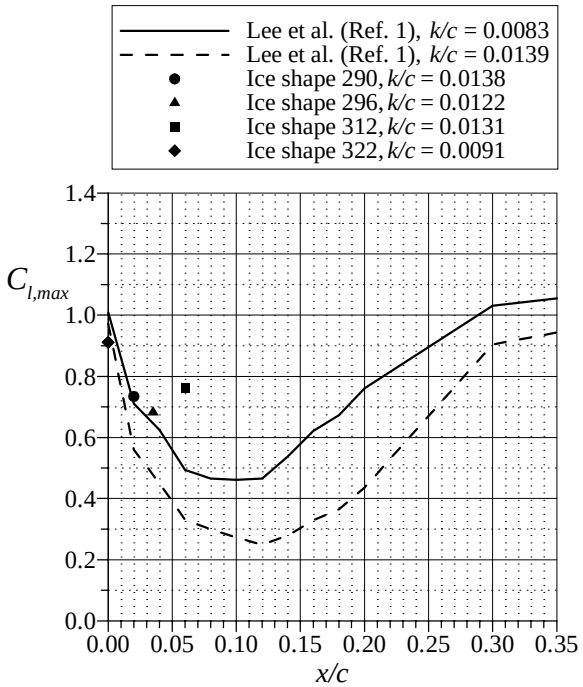

Fig. 31 Comparison of maximum lift data from the present study (at $Re = 7.5\times10^6$, $Ma = 0.21$) with data from Lee et al.[1] (at $Re = 1.8\times10^6$, $Ma = 0.18$)

SUMMARY AND CONCLUSIONS

The objectives of this study were to characterize the nature of residual and intercycle ice accretions, measure the resulting aerodynamic performance penalties of selected intercycle ice accretions and determine if more detailed study was warranted. Ice accretion testing was carried out using a 36-inch chord NACA 23012 airfoil model equipped with a pneumatic deicer. The icing runs were performed at several different cloud conditions modeled after FAR 25 Appendix C. The nominal Reynolds and Mach numbers were 6.5×10^6 and 0.27, respectively. Residual and intercycle ice accretions were generated for zero and four degrees angle of attack. These accretions were documented after several deicer cycles to ensure that "steady state" had been achieved. In select cases, molds were made of the accretions that were later converted into castings for aerodynamic testing. The aerodynamic performance testing was carried out using a similar 36-inch chord NACA 23012 airfoil model over a large range of Reynolds and Mach numbers. A total of four different intercycle ice castings were tested along with the clean configuration. In addition, tests were also conducted with uniformly distributed roughness in the form of 40 and 80-grit sandpaper applied to the airfoil leading edge.

The results of the ice accretion testing showed that the pneumatic deicer generally cleaned the leading edge well, leaving little residual ice. Therefore, the intercycle accretions tended to have more ice on the leading edge and, in some cases, protuberances on the upper surface. The intercycle ice accretions tended to be very repeatable from run to run, once the cycle process had reached a "steady state" after two or three cycles. A large amount of ice did build up during the three-minute period between deicer cycles for the continuous maximum icing cases. The intercycle shapes for the intermittent maximum cases were generally smaller, owing to the one-minute cycles, despite the higher water loading. A single continuous maximum case was run with one-minute boot cycles and this was found to be very effective in minimizing the size of the intercycle ice accretion. Also, varying the deicer activation time had little effect on the resulting intercycle accretion, for the one case that was tested. This means that the pneumatic deicer was equally effective when activated 11 seconds after the spray was turned as when activated after a quarter-inch of ice was allowed to accrete on the leading edge (252 seconds). Finally, the intercycle ice accretions selected for aerodynamic testing tended to be "worst-case scenarios" having more ice located on the upper

surface. This generally occurred for ice accreted at zero degrees angle of attack and for continuous maximum cases having three-minute deicer cycles.

Aerodynamic testing of the clean NACA 23012 airfoil yielded results that showed good agreement with historical data. Furthermore, the variations in the performance coefficients with Reynolds and Mach number followed expected trends. The maximum lift coefficient increased substantially from about 1.5 to 1.8 as the Reynolds number was increased from 2.0×10^6 to 10.5×10^6 at a nearly constant Mach number of 0.12. Increasing Mach number from 0.12 to 0.28 at constant Reynolds numbers of 7.5×10^6 and 10.5×10^6 resulted in an increase in the lift-curve slope and a decrease in the maximum lift coefficient.

The simulated intercycle ice accretions caused significant airfoil aerodynamic performance degradation. Maximum lift coefficient values were typically reduced about 60% from 1.8 (clean) to 0.7 (iced) and stall angle values were reduced from 17 deg. (clean) to 9 deg. (iced). The minimum drag coefficient increased from 0.007 (clean) to 0.026 (iced). An increase in Reynolds number from 2.0×10^6 to 3.5×10^6 caused a small increase in the lift-curve slope and maximum lift coefficient, while an increase in Reynolds number from 3.5×10^6 to 10.5×10^6 at a constant Mach number of 0.12 had virtually no effect on any of the performance coefficients. An increase in Mach number from 0.12 to 0.28 at a constant Reynolds numbers of 7.5×10^6 and 10.5×10^6 caused the maximum lift coefficient to decrease only slightly.

The performance degradation due to the 40 and 80-grit sandpaper applied to the airfoil leading edge was substantially less than for the ice-shape simulations. Maximum lift values were reduced about 33% from 1.8 (clean) to 1.2 (with sandpaper) and stall angles were reduced from 17 deg. (clean) to 12 deg. (with sandpaper). The minimum drag coefficient increased from 0.007 (clean) to 0.011 (with sandpaper). The sandpaper was not large enough to accurately simulate the nominal heights of the intercycle shapes, as it was smaller by nearly a factor of five. Also the sandpaper did not have the ridge-like features of some of the intercycle ice accretions.

The very large performance degradations associated with the intercycle ice shapes implies that more detailed study is warranted. For example, the performance of the NACA 23012 airfoil used here is known to be very sensitive to ice or other contamination in the leading edge region. The effect of intercycle ice on the performance of other airfoils is largely unknown. Also, the 36-inch chord airfoils used in this study were not representative of a typical wing chord. Therefore, reasonable questions may arise about how the present data would apply to characteristics and resulting performance degradation of ice accretions on a larger scale. This has more to do with the ice accretion geometry, since this paper has shown that Reynolds and Mach number effects on performance are very small in the iced case. Since ice accretions and pneumatic boot operation cannot be scaled reliably, full-scale intercycle ice accretions need to be acquired and tested to accurately determine the aerodynamic performance degradation.

ACKNOWLEDGEMENTS

The success of this large collaborative study is due, in part, to the principle participants from the various organizations. The authors wish to thank Jim Riley and Gene Hill of the FAA, Tom Bond of NASA Glenn and Dave Sweet and Galdemir Botura of BFGoodrich for their key contributions to this research effort. In addition, Tim Hawk and Tammy Langhals of NASA Glenn, Pete Brown and the staff of the BFGoodrich IWT deserve recognition for their efforts during the icing tests and post-test data reduction. The ice-shape castings and pressure instrumentation pieces for the aerodynamic testing were skillfully produced by Phil Beck and Roger Meredith of NASA Glenn. The authors also wish to acknowledge the work of test engineers Pam Phillips and Bill Sewall and the experienced technicians of the NASA Langley LTPT. Finally, the authors at the University of Illinois were supported, in part, under FAA grant DTFA MB 96-6-023, with Jim Riley as the technical monitor.

REFERENCES

1. Lee, S., Kim, H.S., and Bragg, M.B., "Investigation of Factors that Influence Iced-Airfoil Aerodynamics," AIAA Paper 2000-0099, Jan. 2000.

2. Shin, J. and Bond, T.H., "Surface Roughness Due to Residual Ice in the Use of Low Power Deicing Systems," NASA TM-105971, AIAA Paper 93-0031, Jan. 1993.

3. Albright, A.E., Kohlman, D.L., Schweikhard, W.G., and Evanich, P., "Evaluation of a Pneumatic Boot Deicing System on a General Aviation Wing Model," NASA TM-82363, June 1981.

4. Bowden, D.T., "Effect of Pneumatic De-Icers and Ice Formations on Aerodynamic Characteristics of an Airfoil," NACA TN-3564, Feb. 1956.

5. Reichhold, J.D., and Bragg, M.B., "Residual Ice Characteristics and the Resulting Aerodynamic Performance Penalties," NASA AGATE WP4.010, University of Illinois at Urbana-Champaign, May 1998.

6. Jackson, D.G., and Bragg,M.B., "Aerodynamic Performance of an NLF Airfoil with Simulated Ice," AIAA Paper 99-0373, Jan. 1999.

7. Hill, E.G., "Airplane Deicing Ice Protection Systems, Deicing Boot Ice Bridging, and Airplane Operating Procedures During In-Flight Icing Conditions," Federal Aviation Administration Transportation Airplane Directorate, Feb. 1999.

8. Hill, E.G., and Reehorst, A.L. (eds.), "FAA/NASA Deicing Boot Ice Bridging Workshop Proceedings," Ohio Aerospace Institute, Cleveland, OH, Nov. 19, 1997.

9. Riley, J.T., Rios, M.A., Rios, Anderson, D., and Dumont, C.J., "A Study of Inter-cycle, Residual and Pre-activation Ice," AIAA Paper 2001-0089, Jan. 2001.

10. Von Doenhoff, A.E., and Abbot, F.T., Jr., "The Langley Two-Dimensional Low-Turbulence Pressure Tunnel," NACA TN 1283, May 1947.

11. McGhee, R.J., Beasley, W.D., and Foster, J.M., "Recent Modifications and Calibration of the Langley Low-Turbulence Pressure Tunnel," NASA TP 2328, July 1984.

12. Paschal, K, Goodman, W., McGhee, R., Walker, B., and Wilcox, P.A., "Evaluation of Tunnel Sidewall Boundary-Layer-Control Systems for High-Lift Airfoil Testing," AIAA Paper 91-3243, Sept. 1991.

13. Allen, H.J., and Vincenti, W.G., "Wall Interference in a Two-Dimensional-Flow Wind Tunnel, with Consideration of the Effect of Compressibility," NACA Report No. 782, 1944.

14. Barlow, J.B., Rae, W.H., Jr., and Pope, A., *Low-Speed Wind Tunnel Testing*, 3rd Ed., John Wiley & Sons, Inc., New York, 1999, p. 307.

15. Abbott, I.H., and von Doenhoff, A.E., *Theory of Wing Sections*, Dover Publications, pp. 124-128 and 498-499, 1959.

16. Drela, M., "XFOIL 6.6 User Primer," MIT Aero and Astro Engineering, Mar. 14, 1996.

17. Ladson, C.L., "Effects of Independent Variation of Mach and Reynolds Numbers on the Low-Speed Aerodynamic Characteristics of the NACA 0012 Airfoil Section," NASA TM-4071, Oct. 1988.

18. Morgan, H.L., Jr., Ferris, J.C., and McGhee, R.J., "A Study of High-Lift Airfoils in the Langley Low-Turbulence Pressure Tunnel," NASA TM 89125, July 1987.

19. Addy, H.E., Jr., and Chung, J.J., "A Wind Tunnel Study of Icing Effects on a Natural Laminar Flow Airfoil," AIAA Paper 2000-0095, Jan. 2000.

20. Lee, S., "Effect of Supercooled Large Droplet Icing on Airfoil Aerodynamics," Ph.D. Dissertation, Dept. of Aeronautical and Astronautical Engineering, Univ. of Illinois, Urbana, IL, 2001.

21. Lee, S., and Bragg, M.B., "Effects of Simulated-Spanwise Ice Shapes on Airfoils: Experimental Investigation," AIAA Paper 99-0092, Jan. 1999.

22. Jacobs, E.N., "Airfoil Section Characteristics as Affected by Protuberances," NACA Report No. 446, 1932.